NASA Technical Memorandum 78464

Wing Analysis Using a Transonic Potential Flow Computational Method

P. A. Henne and R. M. Hicks

JULY 1978
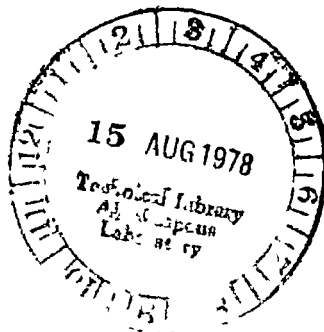
NASA

NASA Technical Memorandum 78464

Wing Analysis Using a Transonic Potential Flow Computational Method

P. A. Henne
McDonnell Douglas Corporation
Long Beach, California

and

R. M. Hicks
Ames Research Center
Moffett Field, California

PAGE MISSING FROM AVAILABLE VERSION

NOMENCLATURE

a nondimensional speed of sound

$\mathcal{R}$ wing aspect ratio, $\dfrac{b^2}{S}$

b wing span, m

C_D drag coefficient, $\dfrac{D}{q_O S}$

C_{D_i} induced drag coefficient

C_{D_S} shock drag coefficient

$\vec{C}_F$ force vector coefficient, $\dfrac{\vec{F}}{q_O S}$

c_d section drag coefficient

c_ℓ section lift coefficient

C_L lift coefficient, $\dfrac{L}{q_O S}$

$C_{L_{\text{exp'd}}}$ exposed wing lift coefficient, $\dfrac{L_{\text{exp'd}}}{q_O S}$

C_p pressure coefficient, $\dfrac{p - p_O}{q_O}$

$\dfrac{c}{4}$ quarter chord, m

D drag

dA differential area, m^2

e span efficiency factor, $\dfrac{C_L{}^2}{\pi \mathcal{R} C_{D_i}}$

$exper$ experimental

$\vec{F}$ force vector

L lift

M_O	free-stream Mach number
$M_\perp$	Mach number normal to a local sweep line
$\hat{n}$	unit normal vector
p	local static pressure, n/m²
p_O	free-stream static pressure, n/m²
q_O	free-stream dynamic pressure, $\frac{1}{2}\rho_O U_O{}^2$, n/m²
$Re_{\bar{c}}$	Reynolds number based on mean aerodynamic chord
S	reference area, m²
$\vec{u}$	nondimensional velocity vector
u,v,w	nondimensional velocity components, $\dfrac{U}{U_O}$, etc.
U,V,W	velocity components, m/sec
U_O	reference free-stream velocity, m/sec
x,y,z	coordinate directions
α	angle of attack, deg
γ	ratio of specific heats
ΔC_{D_c}	incremental drag coefficient due to compressibility
η	wing semispan fraction
λ	wing taper ratio
Λ	wing sweep, deg
ρ	nondimensional local density
ρ_O	free-stream density, kg/m³
∞	infinity conditions
$*$	sonic conditions (calculated using streamwise Mach number)

WING ANALYSIS USING A TRANSONIC POTENTIAL

FLOW COMPUTATIONAL METHOD

P A Henne
McDonnell Douglas Corp , Douglas Aircraft Co

and

R M Hicks
Ames Research Center

SUMMARY

This report summarizes an evaluation of a transonic, full potential flow, computational method for wing analysis The ability of the method to compute wing transonic performance has been determined by applying the method to several different wing designs Comparisons of computed results have been made with both experimental data and results computed by other theoretical procedures Both pressure distributions and aerodynamic forces were evaluated While some inaccuracies were discovered, comparisons indicate that the method is a significant improvement in transonic wing analysis capability In particular, the computational method generally calculated the correct development of three-dimensional pressure distributions from subcritical to transonic conditions Complicated, multiple shocked flows observed experimentally have been reproduced computationally The ability to identify the effects of design modifications has been demonstrated both in terms of pressure distributions and shock drag characteristics The method is applicable to a wider variety of wing configurations, since it solves the full potential equation rather than the small disturbance form of the equation

INTRODUCTION

The aerodynamic design of three-dimensional wings for transonic flight has, until recently, been accomplished primarily by experimental methods Such methods are costly and time consuming compared to theoretical methods However, the development of theoretical transonic methods has been hampered by the complex mathematical character of such flow fields Recently, several computational methods for three-dimensional transonic flows about wings have been developed. This report summarizes an evaluation of Jameson's transonic potential flow solution (ref 1) applied to several different wing designs The objective of the study was to determine the ability of the method to predict transonic wing performance, to determine its range of validity, and to determine faults and deficiencies Particular attention was directed toward the calculation of transonic drag characteristics since such information is of primary importance in the design of efficient wing configurations Using the present computational method a wing can be analyzed in about 1 week

The Jameson code solves the full potential equation Solutions such as that of Bailey and Ballhaus (ref 2) solve a reduced form of this equation consistent with the assumptions of small

disturbances At the time this study was initiated, the intent was to evaluate both the Jameson code and the Bailey and Ballhaus code. However, the available small disturbance code of Bailey and Ballhaus solved an equation which did not include sufficient terms to adequately describe transonic flow about wings with more than 20° to 25° sweep Improvements in this area have been investigated more recently (refs. 3,4) and should provide an improved small disturbance theory for swept wing analyses

· COMPUTATIONAL METHOD

The three-dimensional computational method evaluated in this study is the transonic, potential flow solution of Jameson (FLO22) (ref 1) The method assumes inviscid, adiabatic, and irrotational flow about three-dimensional wings These assumptions are equivalent to assuming isentropic flow. The entropy change through shock waves is neglected The assumption of irrotational flow leads to the existence of a velocity potential, ϕ. The nondimensional velocity components are given by the following derivatives of ϕ

$$u = \frac{U}{U_o} = \phi_x \tag{1}$$

$$v = \frac{V}{U_o} = \phi_y \tag{2}$$

$$w = \frac{W}{U_o} = \phi_z \tag{3}$$

The governing equation for transonic potential flow is written as

$$(a^2 - u^2)\phi_{xx} + (a^2 - v^2)\phi_{yy} + (a^2 - w^2)\phi_{zz} - 2uv\phi_{xy} - 2vw\phi_{yz} - 2uw\phi_{xz} = 0 \tag{4}$$

where a^2 is the square of the nondimensional local speed of sound given by

$$a^2 = \frac{1}{M_o^2} + \frac{\gamma - 1}{2}(1 - u^2 - v^2 - w^2) \tag{5}$$

The Jameson code solves equation (4) for ϕ at a discrete set of mesh points in the space about a wing. Successive line over-relaxation procedures are used to solve a finite difference equation simulating the governing, nonlinear, differential equation The solution is accomplished in a computational space defined by unwrapping and flattening the wing surface with a sheared-parabolic transformation. Equal mesh spacing in the computation plane provides a high concentration of mesh points near the leading edge and a low concentration of points near the trailing edge in the physical space. The mesh in the physical space is shown in figure 1. The concentration of mesh points near the leading edge is a numerical advantage, while the sparse distribution of mesh points near the trailing edge is a disadvantage The details of the finite difference solution scheme are beyond the scope of this report and can be found elsewhere in the literature (refs 1,5)

The original Jameson code used a first-order accurate finite difference scheme to impose the plane of symmetry boundary conditions During the course of this study a second-order accurate boundary condition scheme became available Computed results with the first boundary condition are labeled with an (L), and results with the second boundary condition are labeled (H) Using both schemes, several solutions were computed for comparison purposes and will be presented

An important aspect of solution accuracy with such numerical methods is the number of mesh points. Table I summarizes a description of the meshes used in this study Each of the coarser meshes was used to converge the solution and provide an initial solution for the next finer mesh. Included in the table are the number of iterations typically required to achieve a satisfactory residual or error level Definition of an adequate error level is subjective and depends upon the type of study being carried out For the present study, the number of sonic points in the mesh and the level of the circulation were used in addition to residual level as indications of solution convergence The solution was judged to be sufficiently converged when the rate of change of these parameters became small, typically, this rate was significantly less than 0 1% per iteration near convergence

The three-dimensional transonic flow results presented in this report were calculated on the NASA-Ames CDC-7600 computer. Most of the calculations were completed in 2 weeks Nearly 100 flow solutions were computed, and no programming logic problems or solution convergence problems were encountered

EVALUATION OF AERODYNAMIC FORCES

Although the solutions are inviscid, induced drag and shock drag can be calculated subject to the assumptions of irrotational flow Since the calculated flow is three-dimensional and lifting, a vortex wake extends from the wing to downstream infinity and introduces vortex or induced drag. The method also calculates flow discontinuities representing shock waves Despite the assumption of isentropic flow, however, shock drag can be evaluated from isentropic equations as shown in reference 6 The existence of isentropic shock drag is a result of not conserving momentum normal to the shock surface The momentum of the flow through an isentropic shock is increased, that is, an isentropic shock introduces an upstream or thrust force acting on the system within the flow. In an unbounded, *two*-dimensional isentropic flow the net drag force on the system (shock plus body) within the flow must be zero. Hence, the thrust introduced at the shock discontinuity must be balanced by a drag of equal magnitude on the body In an unbounded, *three*-dimensional isentropic flow the net drag force is not necessarily zero If a wing in the flow is lifting, a vortex wake introduces induced drag Hence, the net drag force on a three-dimensional system (shock plus body) within an isentropic flow is induced drag If shock waves are present, then the drag on the body includes both induced drag and shock drag The shock drag just balances the thrust introduced by the isentropic shocks, and the net drag on the system remains the induced drag

Traditionally, inviscid lift and drag forces are evaluated by integrating surface pressure distributions However, off-the-body momentum control volume integrations are advantageous to flow solutions utilizing points in the field Since the flow at each mesh point is computed during the solution process, this information is readily available for any integration scheme Reference 8 describes applications of such an approach for airfoil analyses

3

A control volume integration is particularly attractive for computed three-dimensional transonic potential flows since control volumes can be constructed to isolate induced drag and shock drag This separation is accomplished by using the characteristics of isentropic shock waves discussed earlier For three-dimensional isentropic flows, a control volume enclosing both the body and any shock waves can only identify induced drag, C_{D_I}. On the other hand, a control volume enclosing just the shock waves can only identify the thrust introduced by the isentropic shock Considering figure 2, the momentum equation for steady, inviscid flows can be written as

$$\vec{C}_F = \frac{\vec{F}}{(1/2)\rho_0 U_0^2 S} = -\frac{2}{S} \iint \left(\frac{C_p}{2} \hat{n} + \rho \vec{u} \vec{u} \cdot \hat{n} \right) dA \tag{6}$$

For the present study the forces are limited to lift and drag, and C_F can be written as

$$\vec{C}_F = C_D \hat{i} + C_L \hat{k} \tag{7}$$

Equation (6) can be split by finding the scalar product in the i and k directions. This operation gives

$$C_L = -\frac{2}{S} \iint \left(\frac{C_p}{2} \hat{k} + \rho \vec{u} \vec{u} \cdot \hat{k} \right) \cdot \hat{n} \, dA \tag{8}$$

and

$$C_D = -\frac{2}{S} \iint \left(\frac{C_p}{2} \hat{i} + \rho \vec{u} \vec{u} \cdot \hat{i} \right) \cdot \hat{n} \, dA \tag{9}$$

If the control volume surface is collapsed to the surface of the body, the boundary condition requires $\vec{u} \cdot \hat{n} = 0$ and equations (8) and (9) reduce to the more familiar surface pressure integrals

The momentum analysis leading to equation (6) is sufficiently general to account for the effects of any net mass flux within the control volume. Hence, any nonconservation of mass due to numerical differencing or convergence tolerances can introduce a fictitious momentum increment that is undesirable The net force on a mass source or sink within a control volume can be shown to be the mass flux multiplied by the free-stream velocity This force acts in the free-stream or thrust and drag direction. To correct for this force, equation (9) can be adjusted by

$$\Delta C_D = \frac{2}{S} \iint \rho \vec{u} \cdot \hat{n} \, dA \tag{10}$$

to give a corrected drag equation written as

$$C_D = -\frac{2}{S} \iint \left[\frac{C_p}{2} \hat{i} + \rho \vec{u} (\vec{u} \cdot \hat{i} - 1) \right] \cdot \hat{n} \, dA \tag{11}$$

A control volume integration based on equations (8) and (11) was evaluated in the transonic potential flow code The results of these evaluations are described in the section entitled

4

Comparison of Calculated and Experimental Aerodynamic Forces Figure 3 illustrates the arrangement of two different control volumes used for the integration Control volume surface A was used to evaluate equations (8) and (11) for lift and induced drag By adding surface B to surface A the wing is excluded from the control volume Only the shock wave or waves remain in the control volume. Equation (11) then provides an evaluation of the isentropic shock thrust which has the same magnitude but opposite sign as the shock drag, C_{D_S}, felt by the wing

CASE GEOMETRY DESCRIPTIONS

Six wing geometries were selected for analysis, including both simple and complicated designs The simple wing configurations provide fundamental comparisons with other theoretical methods, while the more complicated wing designs provide a number of different comparisons with experimental and other theoretical results

Table II is a summary of the characteristics of each wing case. Cases 1 and 2 are unswept, untapered, and untwisted wings with an aspect ratio of 10. The airfoil section is an NACA 0010 for case 1 and an NACA 0020 for case 2 While no experimental results are known to exist for these geometries, the wings provide reasonably two-dimensional flow in the center of the wing where comparisons are made between computed three-dimensional results and results from proven two-dimensional methods (ref 9) Case 3 is a swept, tapered wing that was tested as a wing-out-of-a-wall by the NACA (ref 10). The wing has an NACA 64_1212 airfoil section normal to the leading edge. Case 4 is a swept, tapered, and twisted wing tested by Douglas Aircraft Company The wing has conventional type airfoil sections Cases 5 and 6 are also swept, tapered, and twisted wings but have supercritical airfoil sections These wings were tested in a cooperative program between NASA-Ames Research Center and the Douglas Aircraft Company. Cases 5 and 6 have the same planform but have different airfoil sections The leading edge of case 5 was modified to develop the airfoil sections for case 6.

Cases 4, 5, and 6 are all low-wing designs tested with fuselages and aft sting arrangements Since the computational method is for wings alone, the exposed wings were used for these cases The geometries were set up with the wing-fuselage intersection translated to the centerline of the computational mesh While this representation does not provide the correct wing span, the side of the fuselage and fillet is reasonably flat above the wing, and the wall boundary condition provides an approximate modeling of this area It must be recognized, however, that fuselage flow-field disturbances due to incidence and cross section are not included in the computational method

For the wings with available experimental results, a boundary-layer displacement thickness was added to the input geometries for the computational methods The boundary layers were computed at one subcritical condition and were frozen for all other conditions The Cebeci two-dimensional boundary-layer method (ref 11) was used in conjunction with the Garabedian and Korn two-dimensional flow solution (ref 9) and simple sweep theory The displacement thickness for each defining airfoil section was computed in a strip fashion and modified by an empirical spanwise weighting factor to account for three-dimensional effects This boundary-layer representation is a crude attempt to include viscous effects in the computed flow solutions Such measures may not be required for wings with conventional airfoil sections, but wings with supercritical airfoil sections are

5

substantially affected by the boundary-layer growth Any theoretical analysis involving supercritical airfoils should include some method of accounting for boundary-layer displacement effects

COMPARISON OF CALCULATED AND EXPERIMENTAL PRESSURE DISTRIBUTIONS

Case 1   Figure 4 illustrates computed pressure distributions for case 1 at three different Mach numbers and $0°$ angle of attack The three-dimensional results are for the centerline ($\eta = 0$) airfoil section The two-dimensional pressure distributions, computed on the same airfoil section using the Garabedian-Korn two-dimensional solution, agree reasonably well at all three Mach numbers The computed shock position in the Jameson solution is farther forward than in the two-dimensional result A small discrepancy in pressure level indicated near the trailing edge is probably related to the larger mesh spacing near the trailing edge in the three-dimensional program

Figure 5 presents pressure distributions calculated by three methods for the same wing The three-dimensional result is for $M = 0 8$ and $2°$ angle of attack Again the pressure distribution along the centerline ($\eta = 0$) is shown for the Jameson three-dimensional result The two two-dimensional results were computed for nearly the same section lift coefficient as the three-dimensional pressure distribution The Jameson two-dimensional solution is analogous to the three-dimensional solution in that a parabolic mapping is used rather than a circle plane mapping as in the Garabedian-Korn solution. While minor differences in the pressure distributions are noted, the agreement between the three different solutions is good This comparison indicates that numerical differences can account for approximately 3% of chord in shock position and 0 04 difference in pressure coefficient

Case 2   Case 2 is similar in planform to case 1 but has an NACA 0020 airfoil section Figure 6 presents computed pressure distributions for this 20% thick wing case at three different Mach numbers and $0°$ angle of attack Again, the three-dimensional results are for the centerline ($\eta = 0$) airfoil section The results shown in this figure are very similar to those shown in figure 4 for the 10% thick wing No apparent sensitivity to airfoil thickness is noted in these cases

Case 3   Case 3 is the first swept wing analyzed Figures 7, 8, and 9 present a series of comparisons between experimental and computed pressure distributions In figure 7 the free-stream Mach number is 0.6 and the angle of attack is $4°$ The flow is entirely subsonic at these conditions Figure 8 is for 0 8 Mach number and $4°$ angle of attack, and at this Mach number the upper surface pressures indicate some supersonic flow In figure 9 the Mach number has been increased to 0 85 and a significant amount of supersonic flow exists on the upper surface The computed and experimental pressure distributions agree reasonably well at all three conditions Figure 10 illustrates the computed and experimental shock location for the flow conditions shown in figure 9. The shock location chosen was the chordwise location of the midpoint of the shock pressure rise Considerable unsweeping of the shock is apparent at both the wing root and wing tip Even in the midwing location the shock sweep is less than the sweep of a constant percent chord line

Figure 11 presents a comparison of pressure distributions for the 55% semispan location of this wing at $M_O = 0.85$ and $4°$ angle of attack The computed three-dimensional distribution has a section lift coefficient of 0 55 The two-dimensional results were computed using simple sweep theory and a quarter-chord normal airfoil section from the three-dimensional wing geometry

6

including the addition of displacement thickness The two-dimensional pressure distributions have an equivalent three-dimensional section lift coefficient of 0 55. The three-dimensional computed shock position is further aft than the two-dimensional location The different shock position is the result of planform effects on shock sweep as shown in figure 10. The effective sweep is less than the quarter-chord sweep The experimental pressures do not show the flow acceleration along the upper surface that is evident in all the computed pressures The lack of acceleration could be related to shock boundary-layer interaction or to poor model surface contour quality (ref 7)

Case 4 Figures 12 through 16 present a series of pressure distribution comparisons for case 4. Figure 12 compares computed and experimental pressure distributions for 0.5 Mach number and 4° angle of attack The flow field is almost entirely subsonic at these conditions The agreement between computed and experimental results is good except for the aft pressure recovery In this region the computed pressures indicate a greater recompression than was measured, which could be attributed to several sources Since the mesh spacing is rather large near the trailing edge, some of the extra recompression could be evidence of numerical error The boundary-layer displacement thickness could also be a problem near the trailing edge The real three-dimensional boundary layer near a swept trailing edge is known to exhibit significant crossflow The two-dimensional analysis used to compute the boundary-layer displacement thickness added to the wing geometry does not provide such details and could lead to the extra recompression near the trailing edge. Finally, it must be remembered that this case was tested with a fuselage The fuselage and its associated fillet tend to elevate the local flow velocities This effect is likely present in the measured pressures and could be another source of the difference between the computed and experimental pressures.

Figure 13 compares computed and measured pressures at 0 7 Mach number and 4° angle of attack. At these conditions the wing flow field near the leading edge is supersonic Both the computed and experimental pressures indicate a region of sharp recompression through a shock

In figure 14 the Mach number has been increased to 0 8 at 4° angle of attack At these conditions a significant amount of supersonic flow is indicated along the upper surface The computed shock position for the outboard stations appear to be 10 to 15% of chord further forward than the experimental pressures show Figures 15 and 16 show similar results for 0.82 and 0.85 Mach numbers and 3° and 2° angles of attack, respectively While the shock position is not correct for this case, the growth of the supersonic region and the level of pressure in the supersonic region are reasonably well computed

In an attempt to identify the cause for the discrepancy between the calculated and experimental shock locations, an analysis of the fuselage flow field was made An axisymmetric representation of the fuselage for this model was used to calculate an axisymmetric off-body flow field in the region of the wing This calculation was accomplished using the Axisymmetric Douglas-Neumann Potential Flow Program (ref 12) Compressibility effects were accounted for with a Goethert type correction This modeling has been shown to be adequate for subcritical axisymmetric flows such as this fuselage case. The calculated off-body Mach-number distribution at the wing half-chord location is shown in figure 17 The results are shown for the fuselage with and without a closed afterbody. The close proximity of the wing to the afterbody subjects the wing to Mach numbers elevated by approximately 0 01. Hence, for a wing-body free-stream Mach number of 0.85, the wing is essentially flying in a Mach number 0 86 flow. This effect could account for some of the discrepancy in shock location for this case

Case 5   Figures 18 through 22 present a series of pressure distribution comparisons for case 5, a supercritical wing design. The results shown in figure 18 are for a Mach number of 0 5 and an angle of attack of 2 06°. Three different solutions are shown The three-dimensional F-N (Friedman-Neumann) results, shown as a dashed line, were computed using a surface source-internal vorticity panel method (ref 13) for incompressible potential flow The three-dimensional F-N flow was calculated for the wing-body geometry. Mach-number effects were approximated using the Goethert correction. Jameson results are shown for both wall boundary condition schemes. The higher order scheme resulted in a lower peak negative pressure coefficient along most of the span, an effect particularly evident at the station next to the fuselage The agreement between the different flow solutions and the experimental results is good.

Figure 19 compares computed and experimental results for 0 7 Mach number and 1 8° angle of attack At this condition the flow along the upper surface near the leading edge is supersonic. A significantly stronger suction peak is indicated by both the Jameson solution and the experimental results for the 25% semispan station

The results shown in figure 20 are for a Mach number of 0 75 and an angle of attack of 2 2°. At these conditions the size of the sonic region has increased as the shock wave has begun to move downstream The section at 25% semispan continues to show a higher suction peak and a stronger shock than other sections on the wing.

The Mach number has been increased to 0 8 for the results shown in figure 21 At these conditions, a complicated shock system is observed in both the computed and experimental results. The accuracy of the wall boundary condition is shown to have a significant effect on the computed results for such conditions Large spanwise velocity gradients at this forked shock condition seem to aggravate the wall boundary condition accuracy problem The higher order solution shows a more highly defined double shock system at the inboard sections

Figure 22 compares results at 0 84 Mach number and 1 85° angle of attack. At these conditions the sonic region extends over a major portion of the upper surface The inboard pressures continue to indicate a double shock At the outboard stations the pressures indicate a supercritical flow with a single shock At this condition the upper surface boundary layer is likely to be separated or near separation at the midspan stations The lack of trailing-edge pressure recovery in the experimental results compared to the previous data is evidence of this effect Again the accuracy of the wall boundary condition is shown to have a significant effect at these highly supercritical conditions

Figures 23 and 24 compare computed and experimental shock locations for the same conditions as shown in figures 21 and 22, respectively The heavy lines are used to emphasize the shock pattern in each case While the shock positions do not agree exactly, the basic character is computed reasonably well The double shock comparison is especially encouraging considering that the computed solution is for a wing alone while the experimental results are for a wing-body combination

Case 6   Figures 25 through 29 present a series of pressure distribution comparisons for case 6, a modification of the case 5 supercritical wing design Again a range of Mach numbers is presented. The results shown in figure 25 are for a Mach number of 0 5 and an angle of attack of 2 0° Good agreement is illustrated except for the level of the outboard suction peak The experimental results

8

for the outboard part of the wing indicate a sharp suction peak The experimental peak C_p has essentially the same level as is shown in figure 18 for case 5 Using proven two-dimensional methods (e.g., Garabedian-Korn) the leading edge of the case 6 geometry was designed to significantly reduce the peak C_p. The reduction is noted between the computed three-dimensional results shown in figures 18 and 25 but not in the experimental results at the outboard stations This comparison suggests that the contours of the case 6 model outboard leading edge may be inaccurate.

Figure 26 compares computed and experimental results for the case 6 geometry at 0.7 Mach number and 2.0° angle of attack. Again the agreement between the two results is good except for the outboard suction peak With the Mach number increased to 0 75 (fig 27), however, the flow near the upper surface leading edge is supersonic. A shock wave terminating this region is particularly apparent at the 25% semispan station.

Figure 28 presents results for 0.8 Mach number and 2 0° angle of attack At these conditions the double shock character of the flow is apparent in both the computed and experimental results. If the results in figure 28 are compared to the results for case 5 in figure 21, a significant reduction in the forward shock strength is noted. The largest effect is noted at the 25% semispan station.

Figure 29 presents a comparison of results at 0.84 Mach number and 2.0° angle of attack. The double shock character of the inboard flow field is identified reasonably well by the computed results At these conditions, the outboard experimental results suggest significant boundary-layer separation as indicated by the lack of trailing-edge pressure recovery for the 65 and 85% semispan stations Still, agreement between calculated and measured results is good.

Figures 30 and 31 compare calculated and experimental shock positions for the conditions shown in figures 28 and 29, respectively The basic character of the experimental shock pattern is reasonably well calculated for this case

A direct comparison of cases 5 and 6 is presented in figure 32 The measured and calculated pressure distributions at the 25% semispan station are shown for 0 7 Mach number and approximately 2.0° angle of attack The large reduction in peak C_p and the attendant shock strength is indicated in both the calculated and the experimental results The peak normal Mach number ($M_\perp$) for case 5 is 1.43 The peak was reduced to a level near 1 1 for case 6 The leading-edge section profiles for cases 5 and 6 are shown in figure 32 for the 25% span station.

COMPARISON OF CALCULATED AND EXPERIMENTAL
AERODYNAMIC FORCES

Case 1 The case 1 lift curve, C_L versus α, computed by three different theoretical methods, is shown in figure 33 The Mach number is 0 5 The Giesing results were computed using a vortex lattice lifting surface method (ref 14) The three-dimensional F-N results were computed using an incompressible potential flow method described in the previous section. Results computed by the Jameson code are also shown. The differences found in this comparison are characteristic of the different methods used to compute the flow solutions The Giesing vortex lattice calculation is a lifting surface theory and, hence, does not include lift effects due to airfoil thickness The three-dimensional F-N solution and the Jameson solution, on the other hand, utilize exact boundary

9

conditions to represent the wing geometry, a practice which provides for thickness effects and results in a higher lift curve slope

Both the lower order and higher order wall boundary conditions were used in the Jameson calculations for this geometry at 0 5 Mach number Essentially no effect of the order of the boundary condition was found Since the spanwise velocity gradients are essentially zero except near the tip of this wing geometry, the result reinforces the idea that the effects of the higher order scheme are most significant when spanwise velocity gradients near the root are large Little difference is shown between the surface pressure integral results (SPI) and the control volume integral results (CVI)

The results shown in figure 33 are completely inviscid Since viscosity effects tend to reduce lift at a given angle of attack, the lifting surface results usually compare well with experimental data because of the opposing effects of thickness and viscosity on lift This situation contributes to the requirement that some modeling of boundary-layer growth should be included in analyses using exact airfoil or wing boundary conditions

Figure 34 illustrates the calculated spanwise variation in section lift coefficient, c_ℓ, for case 1 at 0 5 Mach number and 0.5 C_L Results from the same three theoretical methods are shown, with the elliptical distribution shown for comparison purposes The lift distributions computed by all three methods agree very well The variation from elliptical implies that the induced drag for such a distribution should be somewhat greater than $C_L^2/\pi AR$

The computed induced drag polars for this geometry at Mach 0.5 are shown in figure 35 for all three theoretical methods The Giesing results were computed using a Trefftz-plane drag integration procedure, while the results from the other two theoretical methods were computed using control volume integrations for induced drag The Jameson induced drag polar seems to be optimistic compared to the other results If e is defined as $C_L^2/\pi AR C_{D_i}$, an e of 0.94 to 0 96 seems more realistic than the value near 1 0 predicted by the Jameson method The higher value of e computed by the Jameson solution could be associated with lack of spanwise loading definition near the wing tip compared to the three-dimensional F-N and Giesing solution

Figure 36 presents the computed two-dimensional and three-dimensional shock drag characteristics for the case 1 geometry at 0° angle of attack The drag for the two two-dimensional solutions was computed from surface pressure integrals for the NACA 0010 airfoil section The three-dimensional results were computed using control volume integration and have been corrected by an increment in drag level defined so that the shock drag with entirely subcritical flow is zero. For this geometry, the level correction was on the order of 0 001 It should be noted that the three-dimensional solution for this comparison was computed using the lower order wall boundary condition. Results computed for later geometries suggest that the shock drag level error is much improved with the higher order scheme. Nonetheless, the present comparison between two-dimensional and three-dimensional results indicates the basic transonic drag rise character is reasonably well computed by the three-dimensional code. Compared to the two-dimensional results, the level of the three-dimensional shock drag is somewhat reduced, which is appropriate since the wing sections near the tip experience less shock drag than a two-dimensional airfoil.

Case 2 Figure 37 illustrates the computed shock drag characteristics for case 2 at 0° angle of attack The two-dimensional and three-dimensional results shown are similar to those presented in

10

figure 36 for case 1 A correction was also applied to these results so that the subcritical shock drag was zero. Comparison of figure 37 with figure 36 reveals the expected decrease in drag divergence Mach number with increasing airfoil thickness

Case 3 A comparison of experimental and calculated lift curves for case 3 is shown in figure 38 for Mach numbers of 0 6, 0 8, and 0 85 Good agreement exists between the experimental and calculated results. Deviation at the higher angles is probably due to viscous effects Little difference is indicated between the computed results using surface pressure integration (SPI) and control volume integration (CVI)

Figures 39 and 40 present comparisons of spanwise section lift distributions at 0 6 and 0.8 Mach numbers, respectively The computed results display essentially the same character as the experimental distributions.

The calculated induced drag polars for case 3 are shown in figure 41 These results were computed using the control volume integration Since this wing has no twist, the zero induced drag value at $C_L = 0$ is correct It is interesting that essentially no Mach number effect on the induced drag polar is calculated for this geometry

Figure 42 presents total drag (induced plus shock) polars for this geometry The left-hand polars are the result of surface pressure integration. Since drag levels less than the induced drag of an elliptical loading are unrealistic, the drag level errors in these results are apparent The right-hand polars were computed using the control volume integration The separate calculation of shock drag identified a level correction used to set subcritical shock drag to zero, and the resulting total drag polar is much more reasonable.

A comparison of drag rise characteristics is shown in figure 43, with curves shown for C_L's of 0.0, 0.2, and 0 4. The computed results were matched to the experimental data between 0 6 and 0 7 Mach number to compensate for viscous effects and tunnel interference effects. While differences are noted between the computed and experimental drag rise characteristics, the general agreement is reasonable This result is particularly encouraging in light of the fact that the computed result is essentially inviscid and shock boundary-layer interaction and the attendant effects on drag are ignored

Figure 44 presents a comparison of two-dimensional and three-dimensional calculated results relative to the measured drag rise for a C_L of 0 4 The two-dimensional drag rise was computed using simple sweep theory and a quarter-chord normal airfoil section for this wing The Mach number difference shown between the two-dimensional and three-dimensional drag rise curves represents the calculated reduction in drag divergence Mach number due to three-dimensional effects These three-dimensional effects can be recognized in figure 10 as considerable unsweeping of the shock at both the root and tip

Case 4 Case 4 is the first geometry analyzed that was tested as a wing-fuselage combination It must be remembered that the flow solutions for this and the following geometries were computed using a plane of symmetry at the wing-fuselage intersection

Figure 45 illustrates the spanwise distribution of section lift coefficient for this geometry at 0 85 Mach number One set of test data is for the same angle of attack as the computed results, and

a second set of data from another test is for nearly the same exposed wing C_L In either case the computed distribution agrees reasonably well with the experimental results

Figure 46 illustrates computed induced drag polars for this configuration Again, these results were computed with the control volume integration Both higher and lower order wall boundary condition solutions are included, and little difference is noted between the results for these two representations As was noted in the case 3 results, the Mach number effect on induced drag is again negligible This particular geometry has a significant amount of aerodynamic twist as the computed drag level at $C_L = 0$ indicates

Figure 47 compares experimental and computed drag rise characteristics for case 4. The results are presented as a compressibility drag coefficient increment, ΔC_{D_C} This increment is taken relative to a subcritical Mach number drag level The curve is presented for a total (wing plus fuselage) C_L of 0 5 To make this comparison, the Jameson $C_{L_{exp'd}}$ was augmented by a $C_L/C_{L_{exp'd}}$ ratio computed by the Giesing vortex lattice method The Jameson results were computed using the higher order wall boundary condition The shock drag computed with the lower order scheme proved to be inconsistent for this and the succeeding complicated wing geometries (The improvement due to the higher order scheme is discussed in detail for case 5) Both surface pressure integration and control volume integration results are shown in figure 47. The calculated drag rise characteristics appear to be premature by about 0 02 in Mach number

Case 5 Figure 48 presents a comparison of section lift distributions for case 5 Four theoretical results along with experimental data for this geometry are shown for 0 5 Mach number and 2.06° angle of attack The theories used were Giesing vortex lattice, three-dimensional F-N, and Jameson three-dimensional (H) and three-dimensional (L) It should be noted that the wing geometries, including the boundary-layer displacement surface, for the Jameson solution and the three-dimensional F-N solution were identical The difference between these two solutions in the outboard region of the wing is likely to be associated with numerical accuracy of one or both of these solutions The outboard pressure distributions shown in figure 18 for this case indicate that less aft loading is computed by the Jameson solution than by the three-dimensional F-N solution, a characteristic which accounts for the difference in section lift coefficient The reduced aft loading of the Jameson solution could be associated with reduced mesh definition near the trailing edge The fact that the Jameson solution agrees better with experimental results may be evidence of compensating errors in representing the boundary layer and in the basic inviscid solution near the trailing edge. An increment in c_ℓ is also noted between the (H) and (L) Jameson solutions This increment is associated primarily with the difference in leading-edge suction peaks noted in figure 18

Figure 49 compares section lift distributions for the same geometry at 0 8 Mach number and 2.2° angle of attack. As with the pressure distributions, a significant difference is noted between the (H) and (L) Jameson section lift distributions for this geometry at these flow conditions The higher order solution is closer to the experimental results

Figure 50 presents a comparison of the induced drag polars computed from control volume integration Results are shown for both the lower order and the higher order wall boundary condition, however, little difference is noted Again, no significant Mach number effect is apparent in the induced drag polars.

12

Figure 51, which shows the total drag polars, illustrates the beneficial effect of the higher order wall boundary condition on the calculation of shock drag characteristics. The upper polars are the pressure integration results using the lower order wall boundary condition As can be seen, the drag levels relative to elliptical loading induced drag are unrealistic, and the Mach number trends are inconsistent The lower polars are the pressure integral results using the higher order boundary condition and show much improved characteristics The drag levels are greater than those of an elliptical loading, and the Mach number effects seem more reasonable A similar improvement is observed in the control volume integration results The shock drag calculated by control volume integration requires a C_D level correction of approximately 0.0002 for cases 5 and 6.

Figure 52 compares experimental and computed drag rise characteristics for this geometry Again, the Jameson $C_{L_{exp'd}}$ was augmented to account for fuselage lift carry-over Curves for two C_L's are shown Significant drag creep is noted before drag divergence for this configuration, with greater creep shown by the experimental results than by the computed results This difference is likely to be associated with viscous effects which are not included in the computed characteristics

Case 6 The geometry for case 6 is a relatively small leading-edge modification of case 5. Consequently, little difference is noted in the lift and induced drag characteristics between cases 5 and 6. However, the modification was designed to alter the transonic flow development on the upper surface in an attempt to reduce the drag creep shown in figure 52

Figure 53 compares the experimental and computed drag rise characteristics for case 6 Again, the inviscid computed results tend to underpredict the experimental levels of drag creep A significant reduction in creep is noted in both the experimental and computed characteristics for these results compared to figure 52 at both 0 5 and 0 6 C_L

The difference between the drag levels of cases 5 and 6 is shown versus Mach number in figure 54. This figure is a unique comparison of four different methods of evaluating drag characteristics The experimental results include both force balance and wake rake measurements made during the DAC/NASA-Ames cooperative wind-tunnel test program The computed results include both the pressure integral and control volume integral First, the comparison indicates that the computed differences have the right sign except at the high C_L, high Mach number conditions, where massive boundary-layer separation was observed experimentally. Secondly, the computed differences generally are the correct magnitude The comparison is evidence that considerable confidence is justified in using this computational method to develop and modify wing contours

CONCLUSIONS

The Jameson three-dimensional transonic potential flow program has been thoroughly evaluated Six different wing geometries, including both simple and complicated designs, have been analyzed at numerous flow conditions Momentum control volume integrations were developed which allowed the separate calculation of induced drag and shock drag Viscous effects were roughly modeled using a subcritical, frozen, two-dimensional displacement thickness added to the wing geometry Calculated aerodynamic characteristics have been compared to experimental results and other theoretical results Favorable comparisons of both pressure distributions and aerodynamic

forces indicate that the Jameson method is quite acceptable for transonic wing analysis The following conclusions are emphasized

1 The ability to calculate the correct development of three-dimensional pressure distributions from subcritical to transonic conditions has been demonstrated

2. The correct character of complicated, multiple-shock flows has been calculated by the program

3. The calculated induced drag was found to be insensitive to Mach number for the types of wings analyzed

4 The ability to identify the effects of design modifications has been demonstrated for both pressure distributions and shock drag characteristics

5 The computer code proved reliable, no convergence problems were encountered in nearly 100 different flow solutions

The good agreement is particularly encouraging in light of the successful applications of an essentially inviscid, wing-alone analysis to viscous, wing-body configurations

Ames Research Center
National Aeronautics and Space Administration
Moffett Field, Calif. 94035, February 22, 1978

REFERENCES

1 Jameson, A , and Caughey, D A   Numerical Calculation of the Transonic Flow Past a Swept Wing New York University ERDA Report COO 3077-140, June 1977 NASA CR-153297, 1977

2 Bailey, Frank R , and Ballhaus, William F   Relaxation Methods for Transonic Flow About Wing-Cylinder Combinations and Lifting Swept Wings Proceedings of the Third International Conference on Numerical Methods in Fluid Dynamics, Paris, Vol II, Problems of Fluid Mechanics, July 3–7, 1972 Lecture Notes in Physics, Vol 19, Springer-Verlag, 1973, pp 2–9

3 Ballhaus, W F , Bailey, F R , and Frick, J   Improved Computational Treatment of Transonic Flow About Swept Wings Advan in Eng Sci , vol 4, 1976, pp 1311–1320 NASA CP-2001, 1976

4 Boppe, C W   Calculation of Transonic Wing Flows by Grid Embedding AIAA Paper 77-207, Jan 1977

5 Jameson, Antony   Iterative Solution of Transonic Flows Over Airfoils and Wings, Including Flows at Mach 1 Comm Pure Appl Math , vol 27, no 3, May 1974, pp 283–309

6 Steger, Joseph L , and Baldwin, Barrett S   Shock Waves and Drag in the Numerical Calculation of Isentropic Transonic Flow NASA TN D-6997, Oct 1972

7 Ashley, Holt, and Landahl, Marten   Aerodynamics of Wings and Bodies Addison-Wesley Publishing Company, Reading, Mass , 1965

8 Murman, E M , and Cole, J D   Inviscid Drag at Transonic Speeds AIAA Paper 74-540, June 1974

9 Bauer, F , Garabedian, P , and Korn, D   Theory of Supercritical Wing Sections Springer-Verlag (New York), 1972

10 Edwards, George G , and Boltz, Frederick W   An Analysis of the Forces and Pressure Distribution on a Wing With the Leading Edge Swept Back 37 25° NACA RM A9K01, Mar 1950

11 Keller, Herbert B , and Cebeci, Tuncer   Accurate Numerical Methods for Boundary-Layer Flows II Two-Dimensional Turbulent Flows AIAA J , vol 10, no 9, Sept 1972, pp 1193–1199

12 Hess, J L , and Smith, A M O   Calculation of Potential Flow About Arbitrary Body Shapes Douglas Aircraft Company Report no ES-40622, 1962

13 Friedman, D M   A Three-Dimensional Lifting Potential Flow Program McDonnell-Douglas IRAD Report MDC-J6182/01, 1974

14 Giesing, Joseph P   Lifting Surface Theory for Wing-Fuselage Combinations McDonnell Douglas Report DAC-67212, vol I, Aug 1968
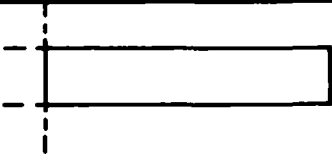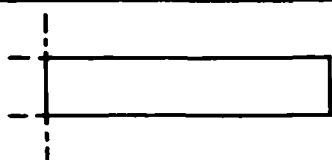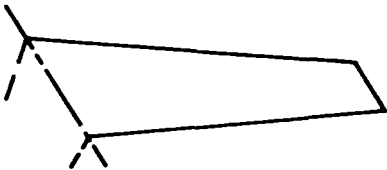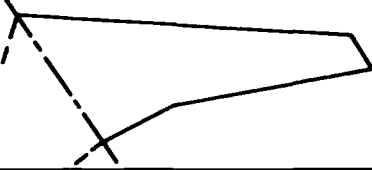
TABLE I – JAMESON PROGRAM MESH AND SOLUTION CHARACTERISTICS

[Total computation time $\cong$ 900 CPU sec on CDC-7600   Nominal residual level $\cong$ 5 0×10^{-5}]

Mesh	Mesh cells NX, NY, NZ	Maximum number[a] streamwise points per airfoil surface	Spanwise stations on wing	Iterations (typical)
1	48, 6, 8	16	6	75
2	96, 12, 16	31	11	75
3	192, 24, 32	61	21	75

[a]Maximum number of streamwise points occurs at maximum chord length station   Streamwise points are reduced along tapering chord

TABLE II – CASE GEOMETRY CHARACTERISTICS

CASE	PLANFORM	SWEEP (c/4), deg	AIRFOILS
1		0	NACA 0010
2		0	NACA 0020
3		35 18	NACA 64_1212 NORMAL SECTION
4		35	CONVENTIONAL
5		32	SUPERCRITICAL
6		32	SUPERCRITICAL (LEADING-EDGE MODIFICATION OF CASE 5)

17

PAGE MISSING FROM AVAILABLE VERSION
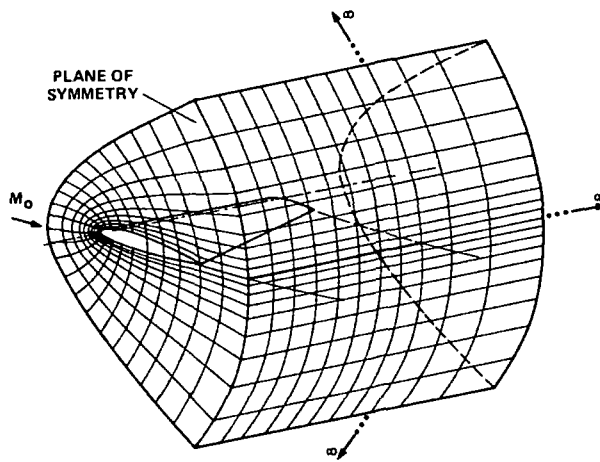
Figure 1 — Sheared parabolic coordinate system used in Jameson three-dimensional transonic flow solution.
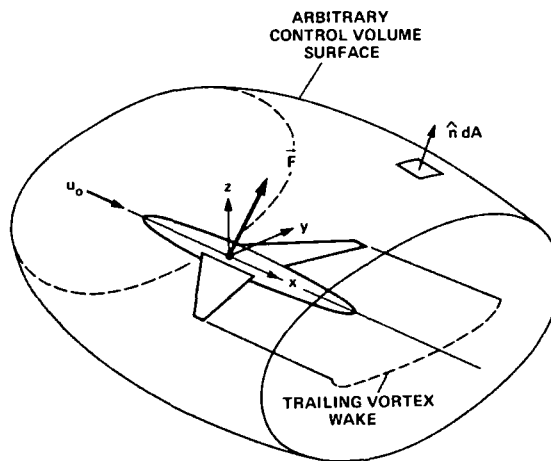
Figure 2 — Momentum control volume and coordinate system
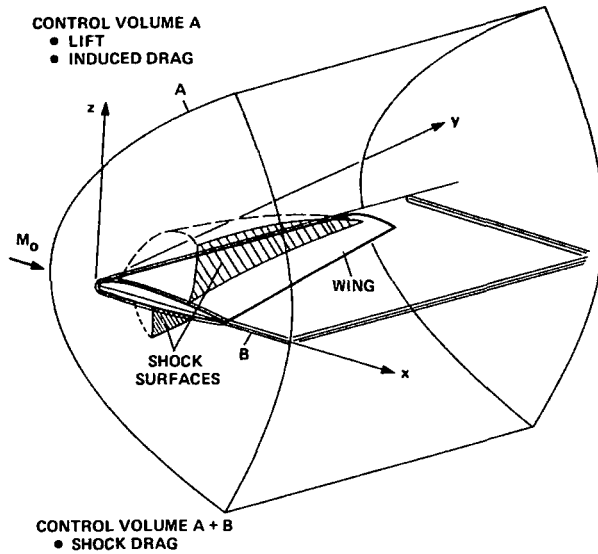
Figure 3 — Momentum control volume used to calculate aerodynamic forces
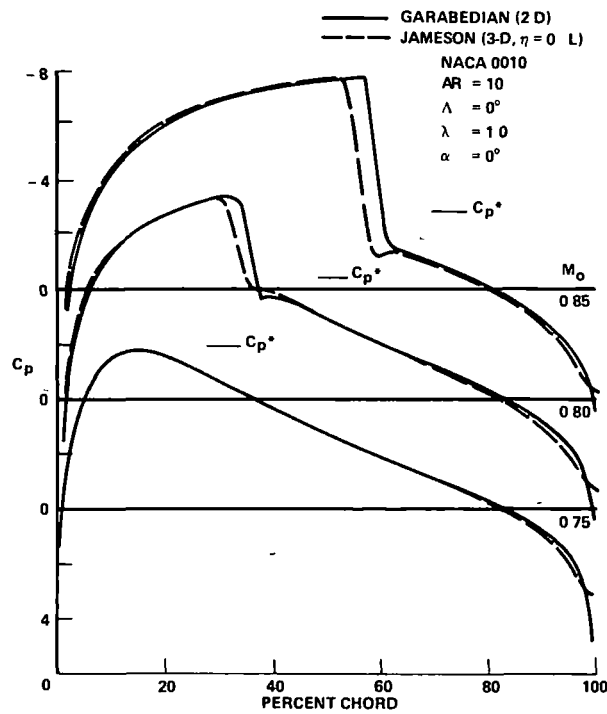
Figure 4 — Comparison of calculated pressure distributions for DAC case 1 at three different Mach numbers

20
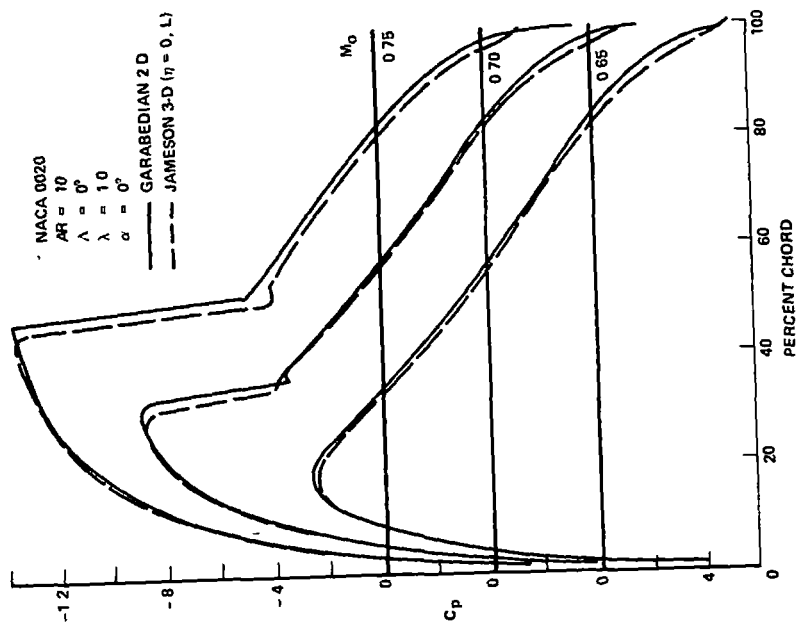
Figure 6 – Comparison of calculated pressure distributions for DAC case 2 at three different Mach numbers.
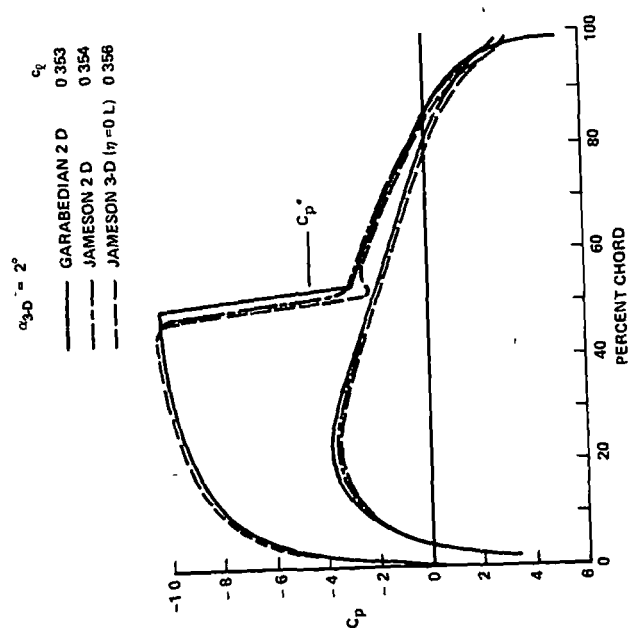
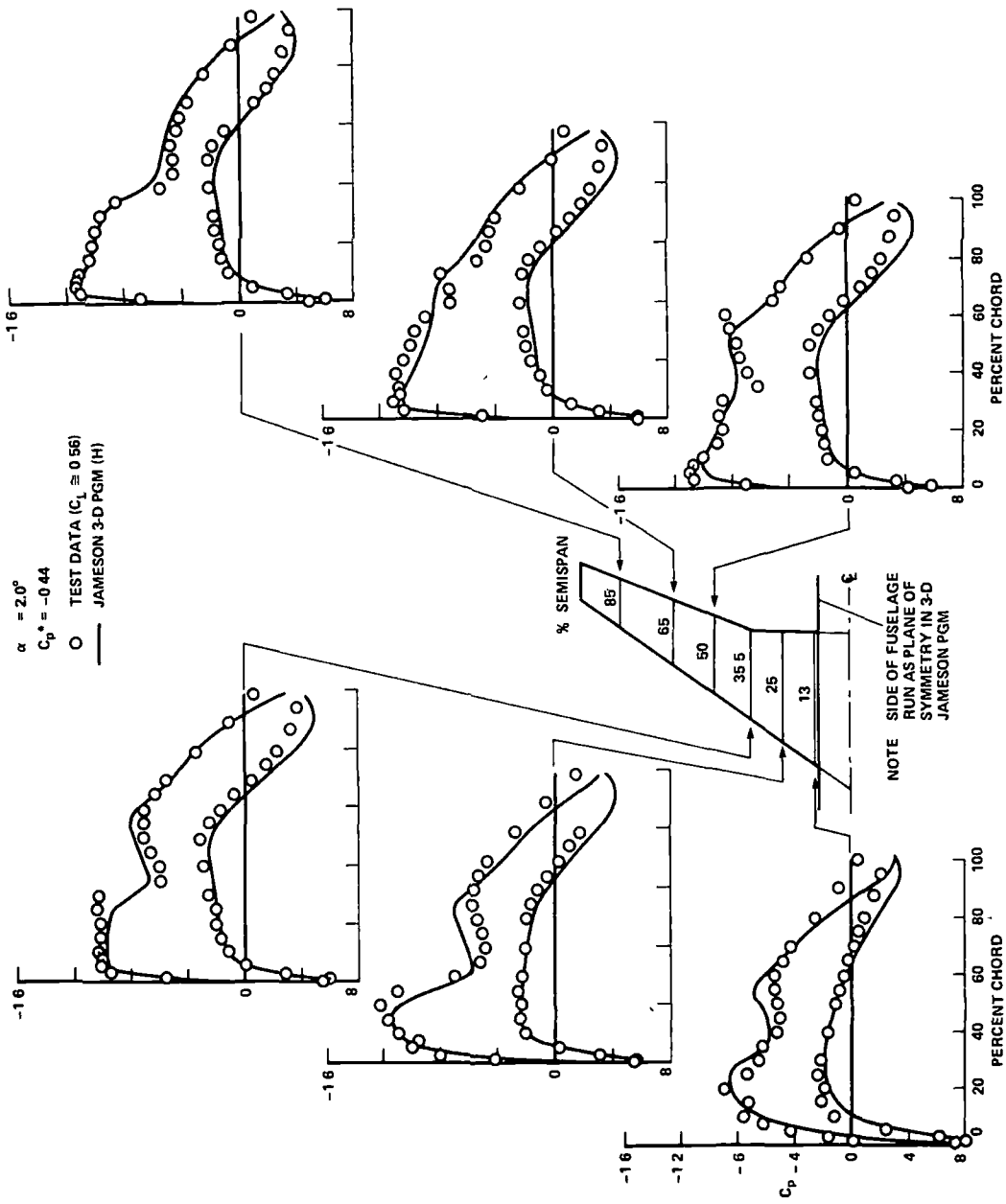Figure 5 – Comparison of calculated pressure distributions for DAC case 1 at 0 8 Mach number
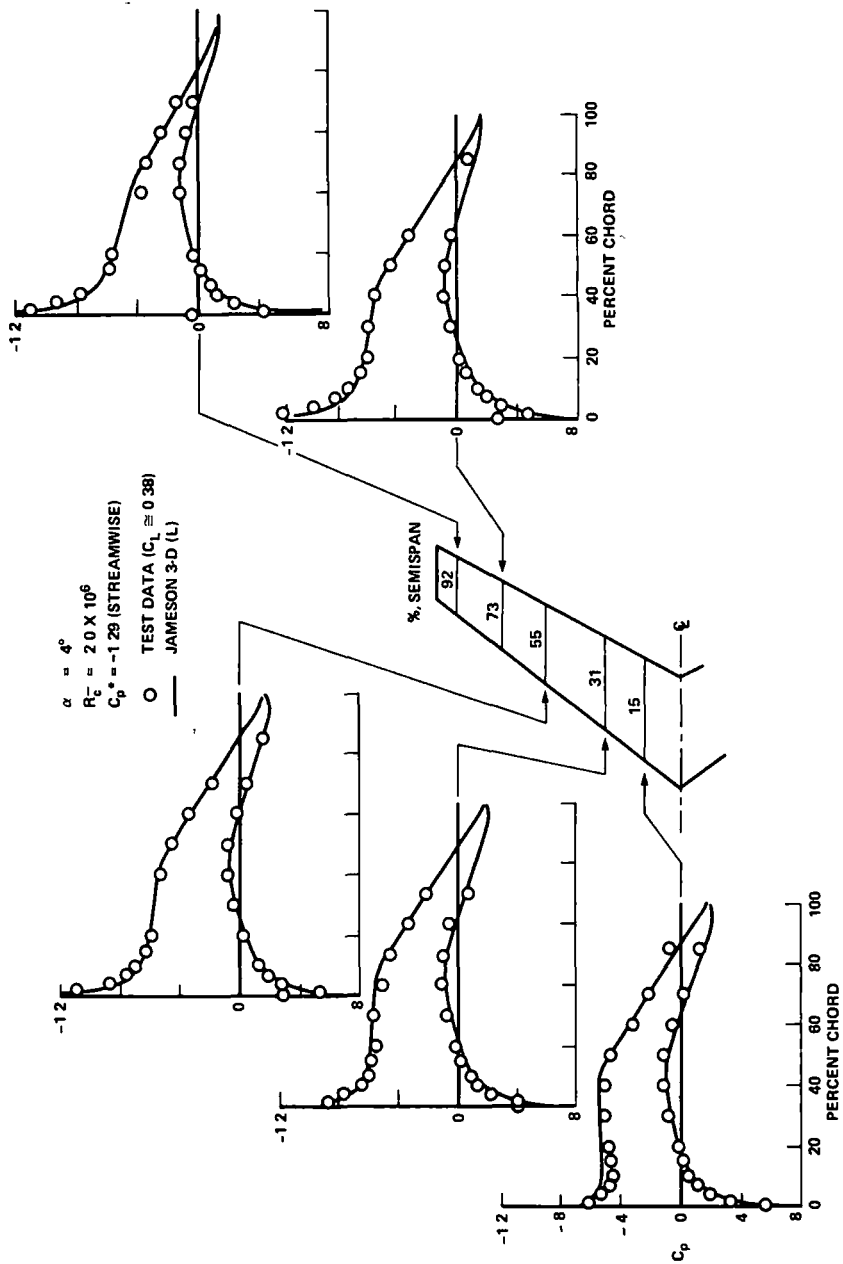
Figure 7.— Comparison of calculated and experimental wing pressure distributions for DAC case 3 at 0.6 Mach number
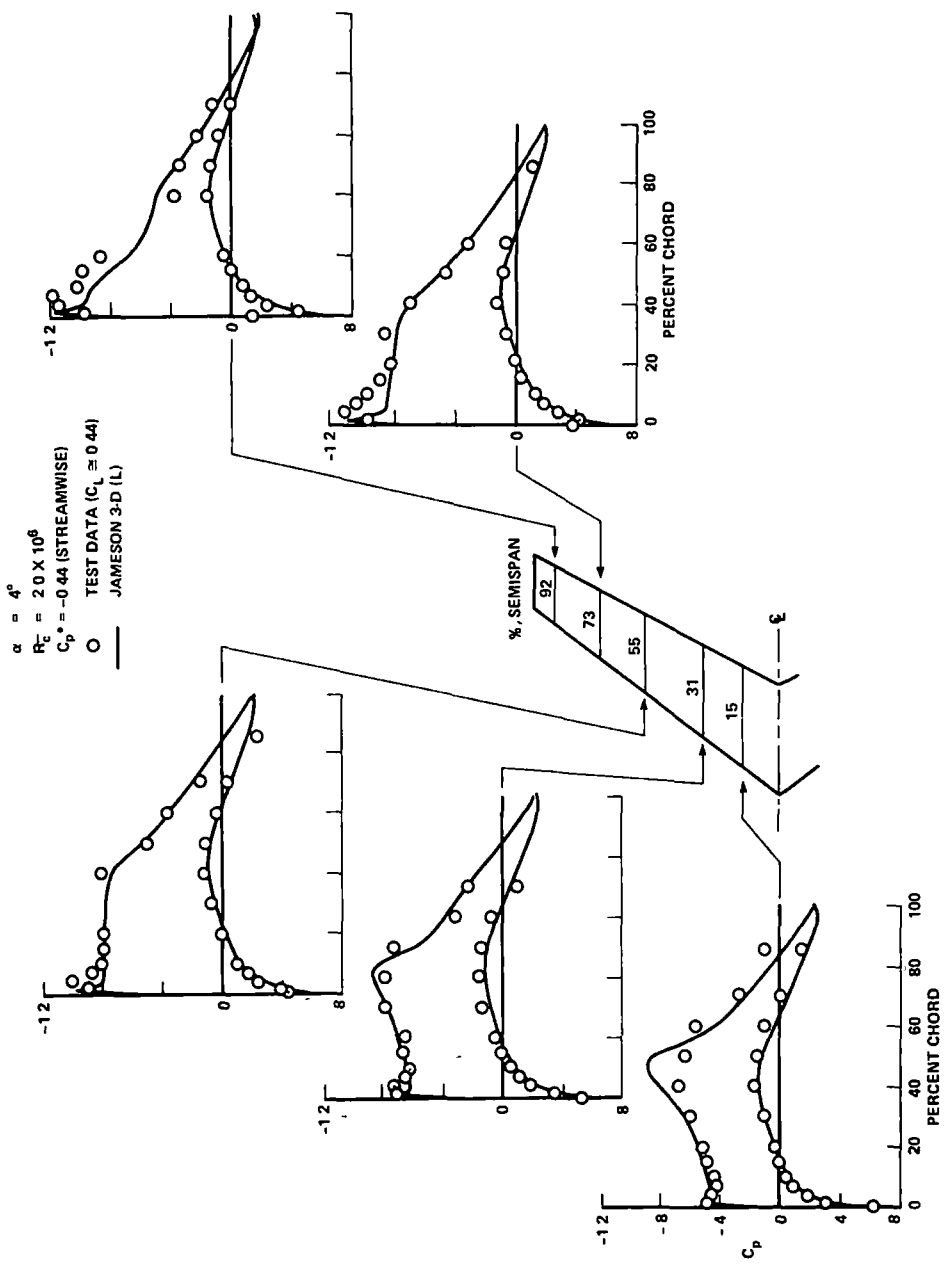
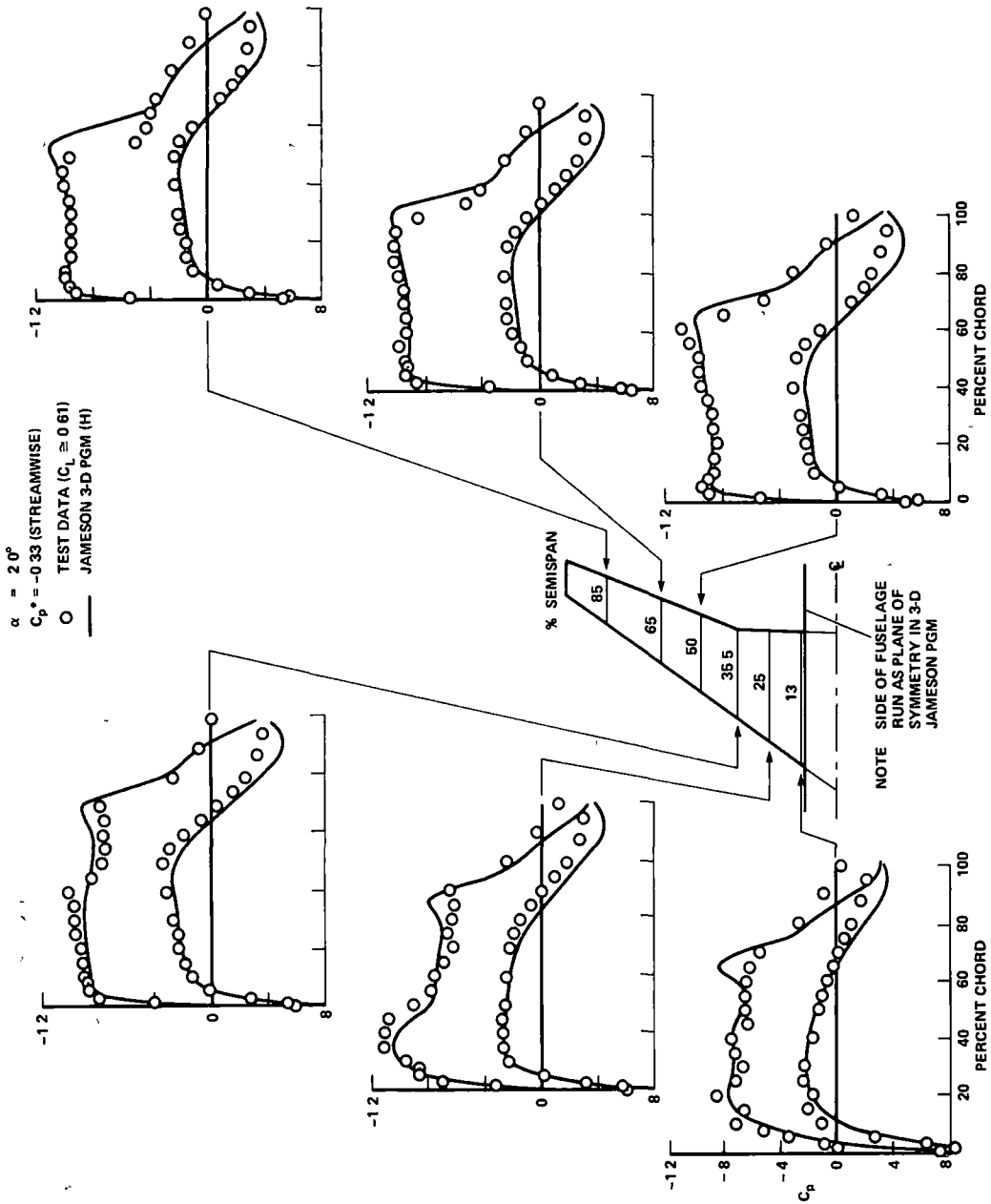Figure 8.— Comparison of calculated and experimental wing pressure distributions for DAC case 3 at 0 8 Mach number
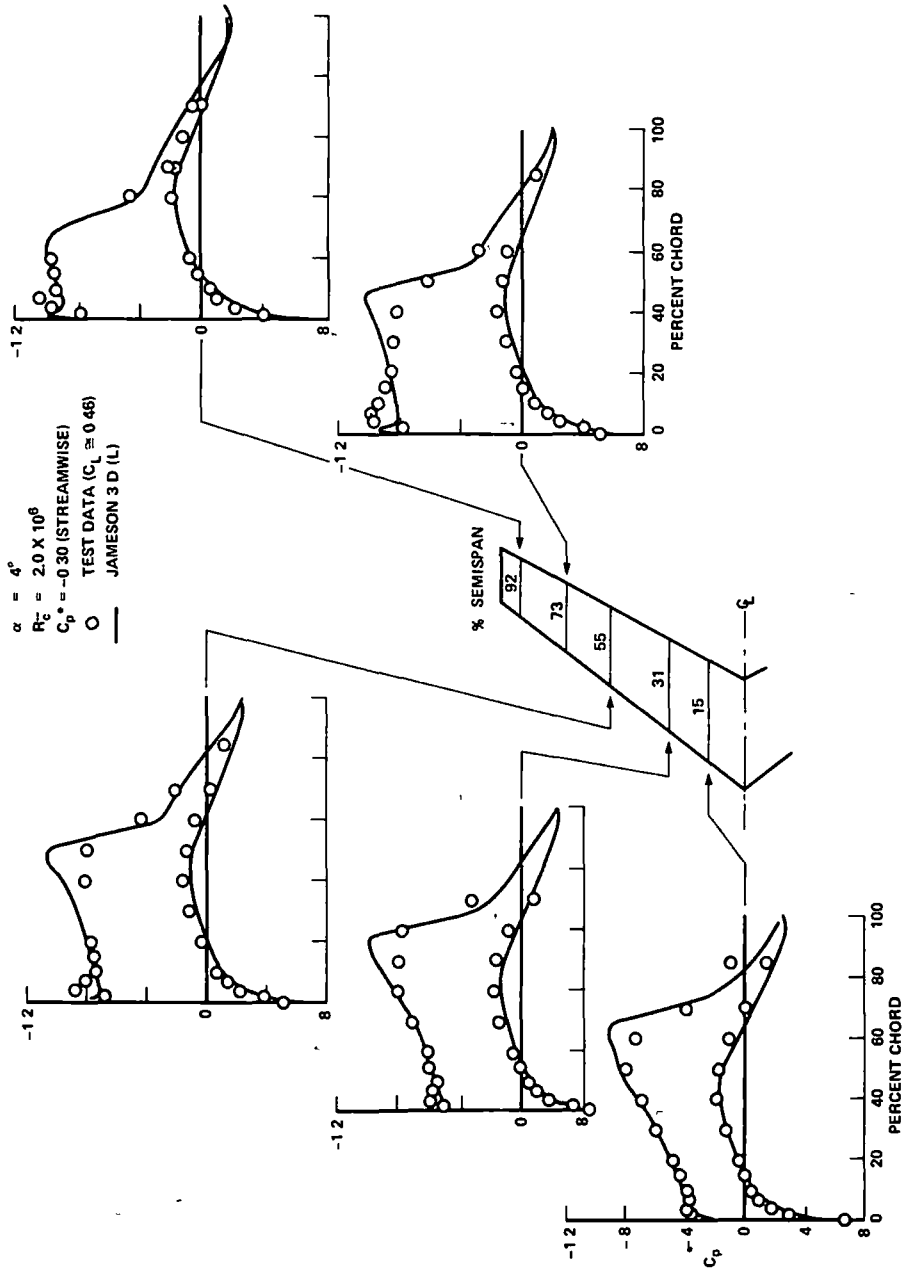
Figure 9 – Comparison of calculated and experimental wing pressure distributions for DAC case 3 at 0 85 Mach number
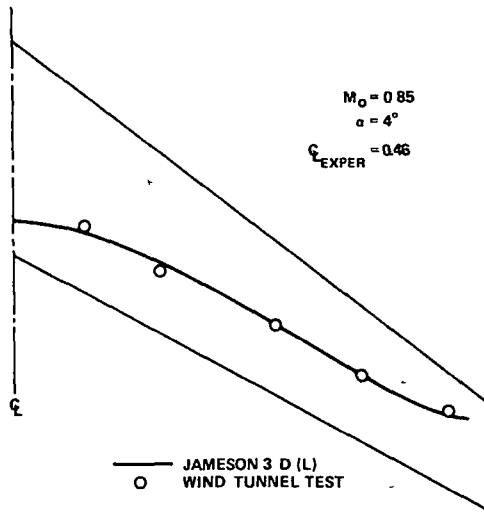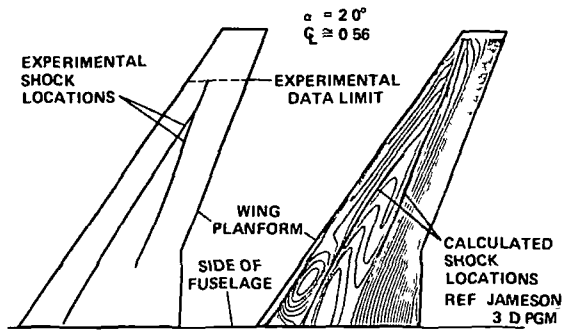
Figure 10 — Comparison of calculated and experimental shock position for DAC case 3
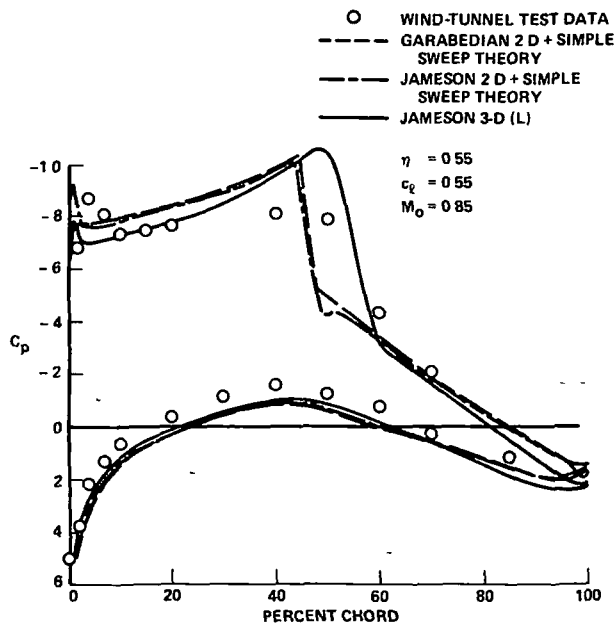
Figure 11 — Comparison of calculated and experimental pressure distributions for DAC case 3
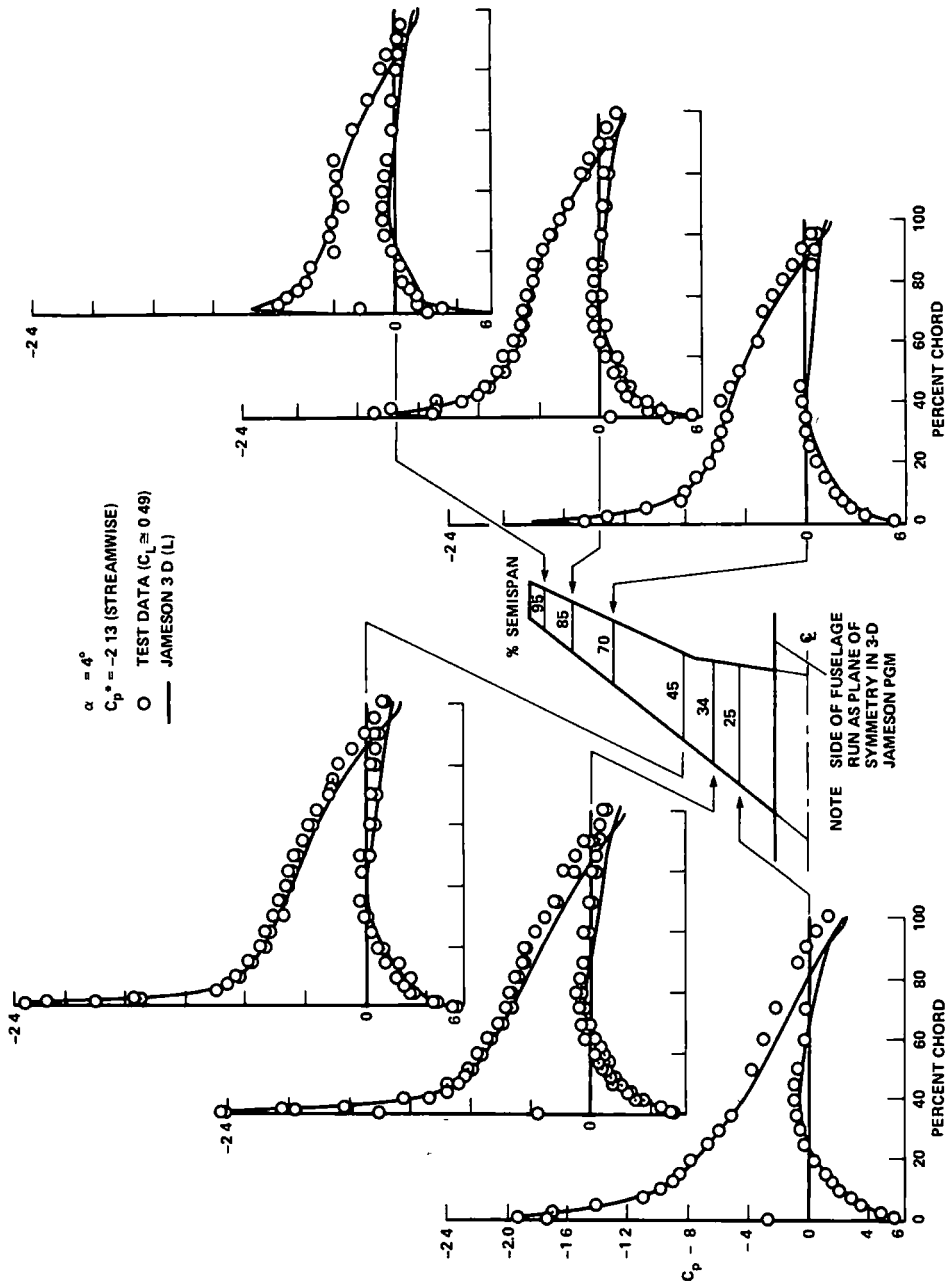
Figure 12.— Comparison of calculated and experimental wing pressure distributions for DAC case 4 at 0 5 Mach number
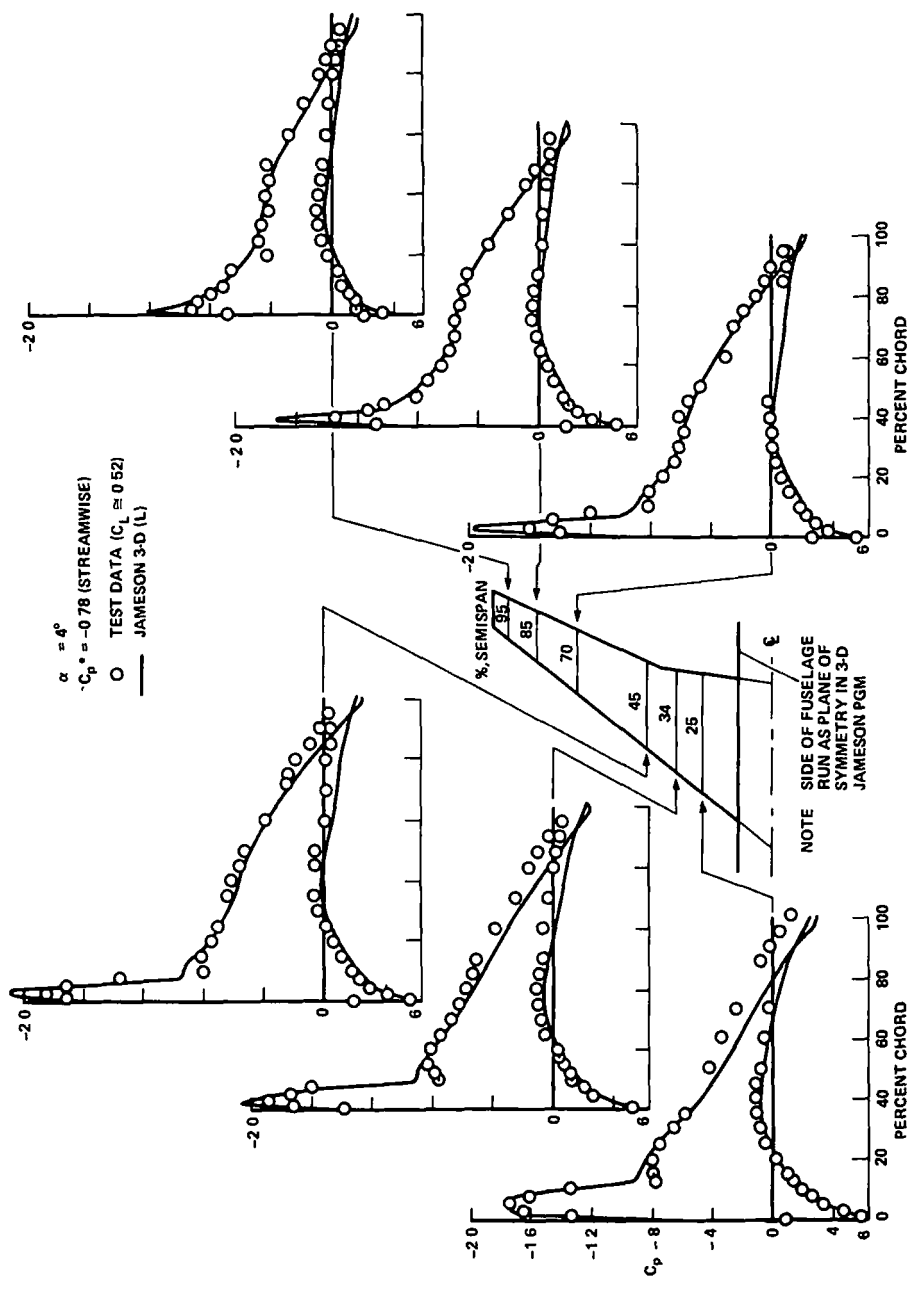
Figure 13 – Comparison of calculated and experimental wing pressure distributions for DAC case 4 at 0 7 Mach number

27
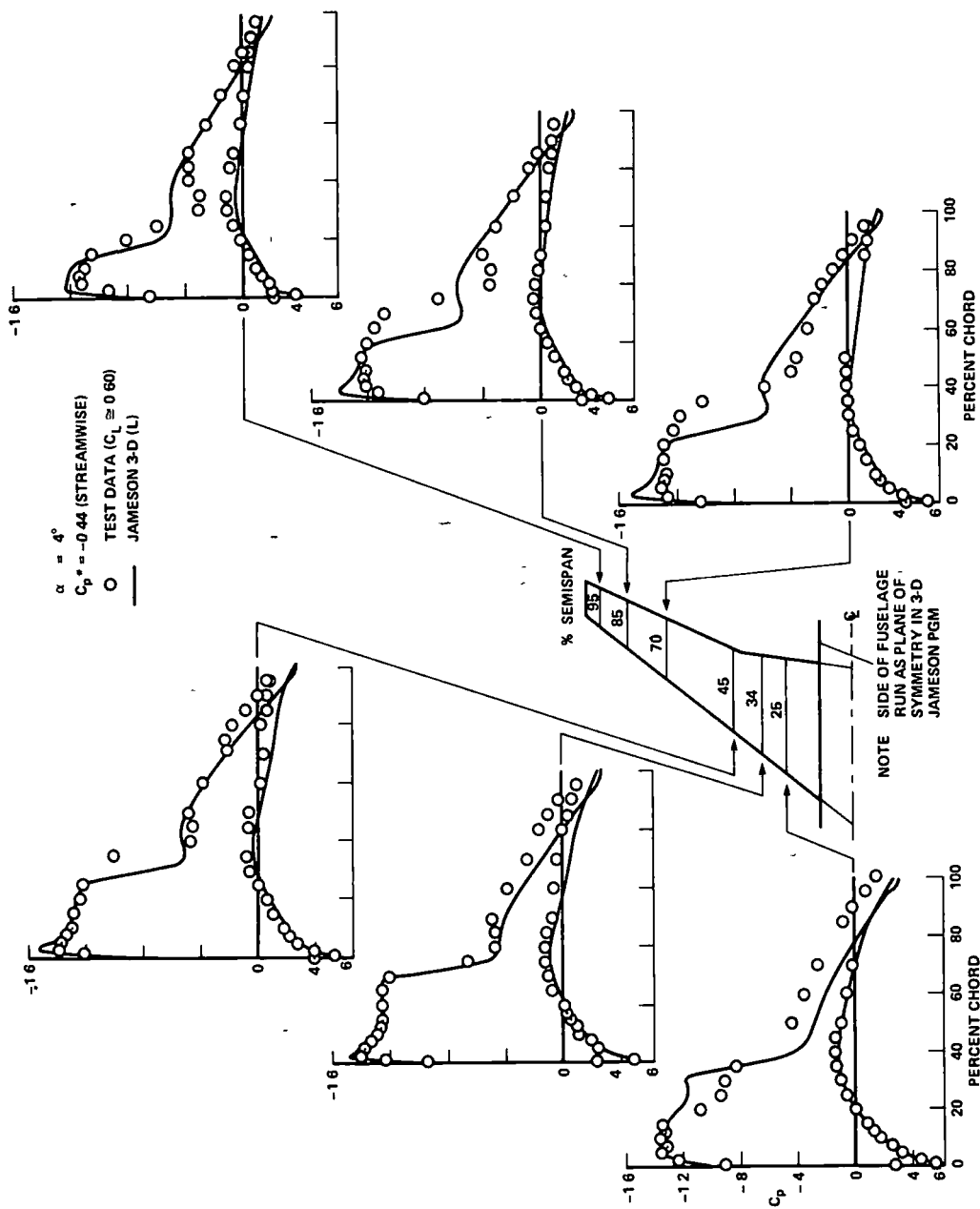
Figure 14.– Comparison of calculated and experimental wing pressure distributions for DAC case 4 at 0 8 Mach number
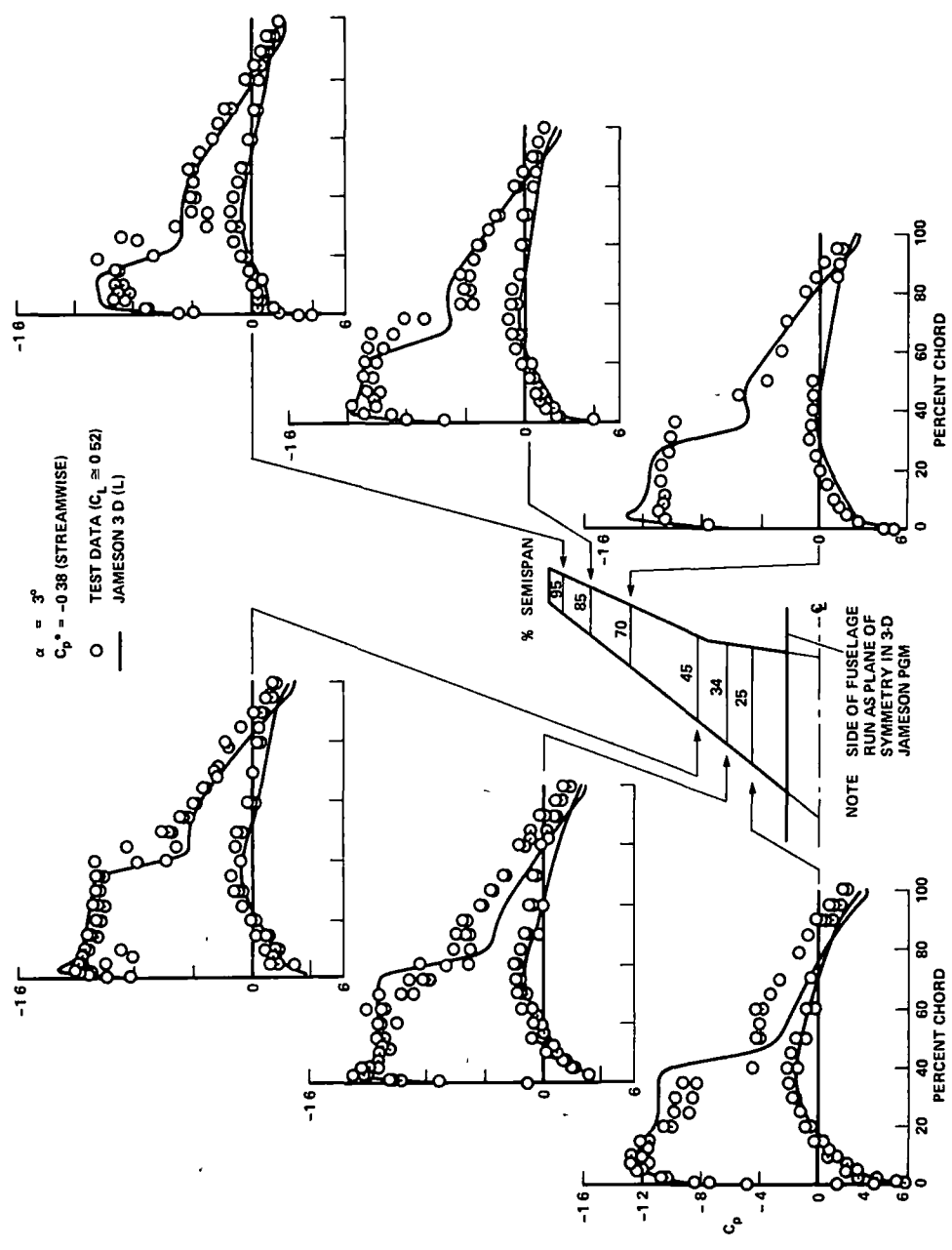
Figure 15.— Comparison of calculated and experimental wing pressure distributions for DAC case 4 at 0 82 Mach number

29
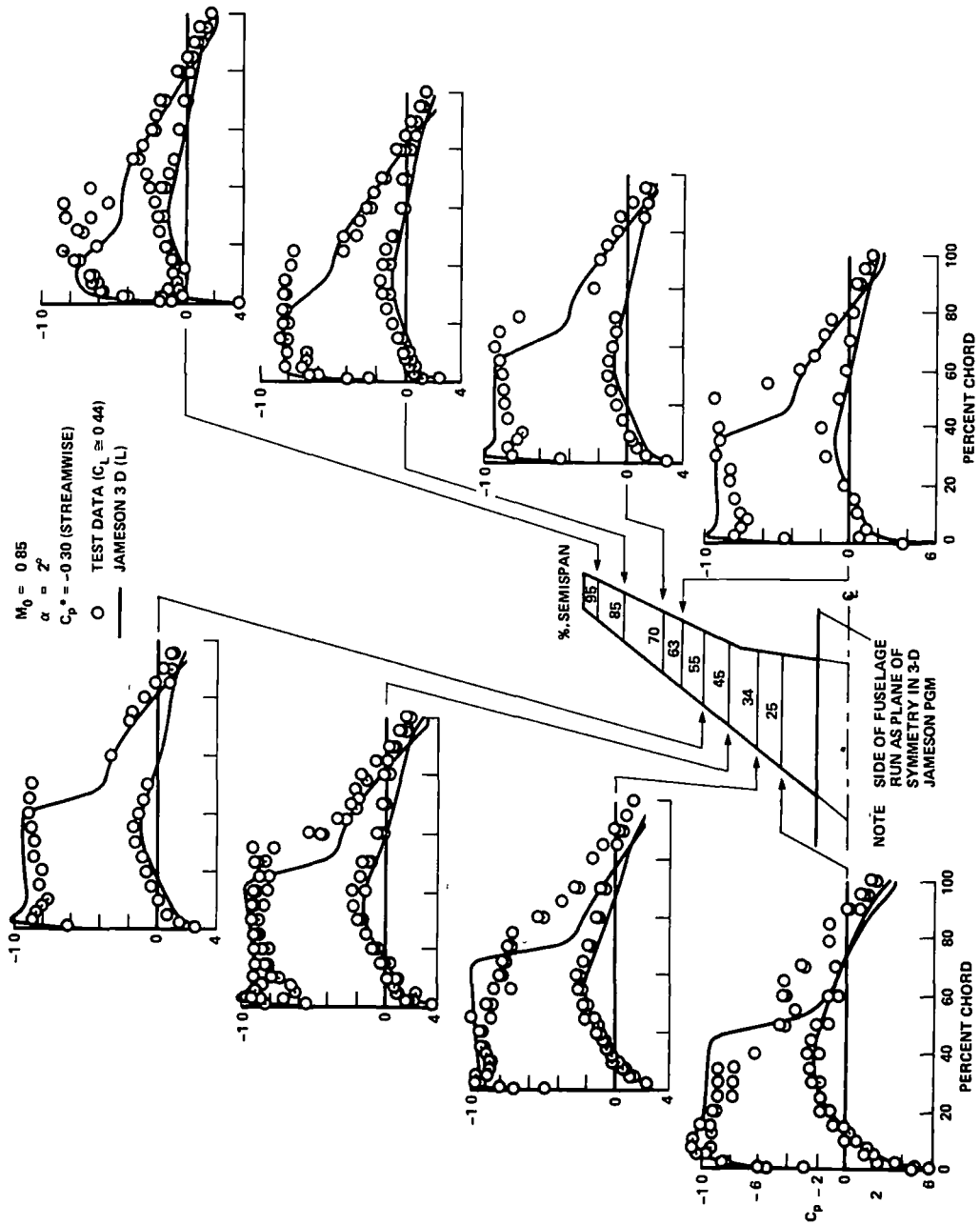
Figure 16.— Comparison of calculated and experimental wing pressure distributions for DAC case 4 at 0 85 Mach number
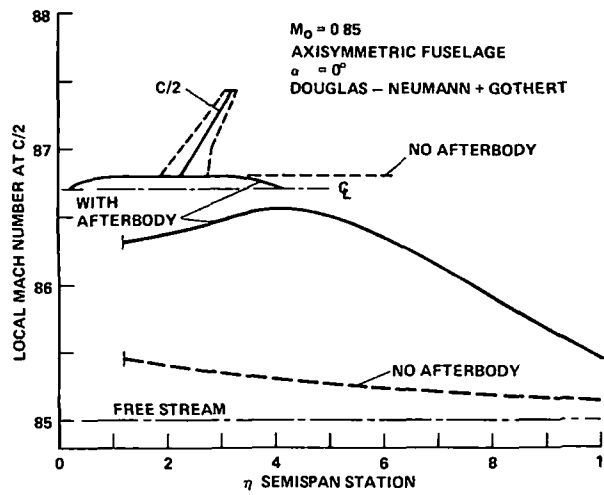
Figure 17 — Estimated spanwise variation of local Mach number due to fuselage nose and afterbody for DAC case 4
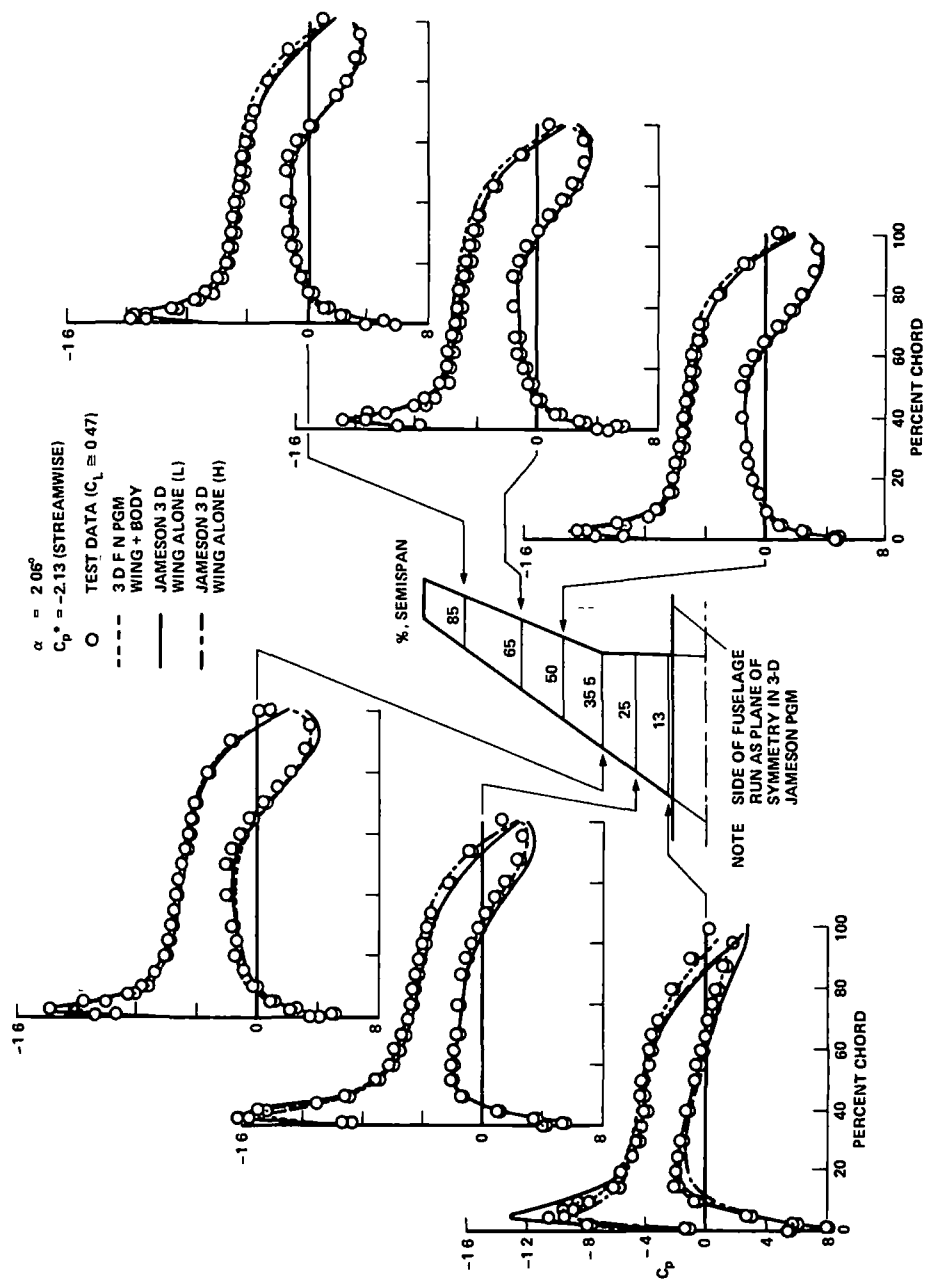
Figure 18 – Comparison of calculated and experimental wing pressure distributions for DAC case 5 at 0 5 Mach number
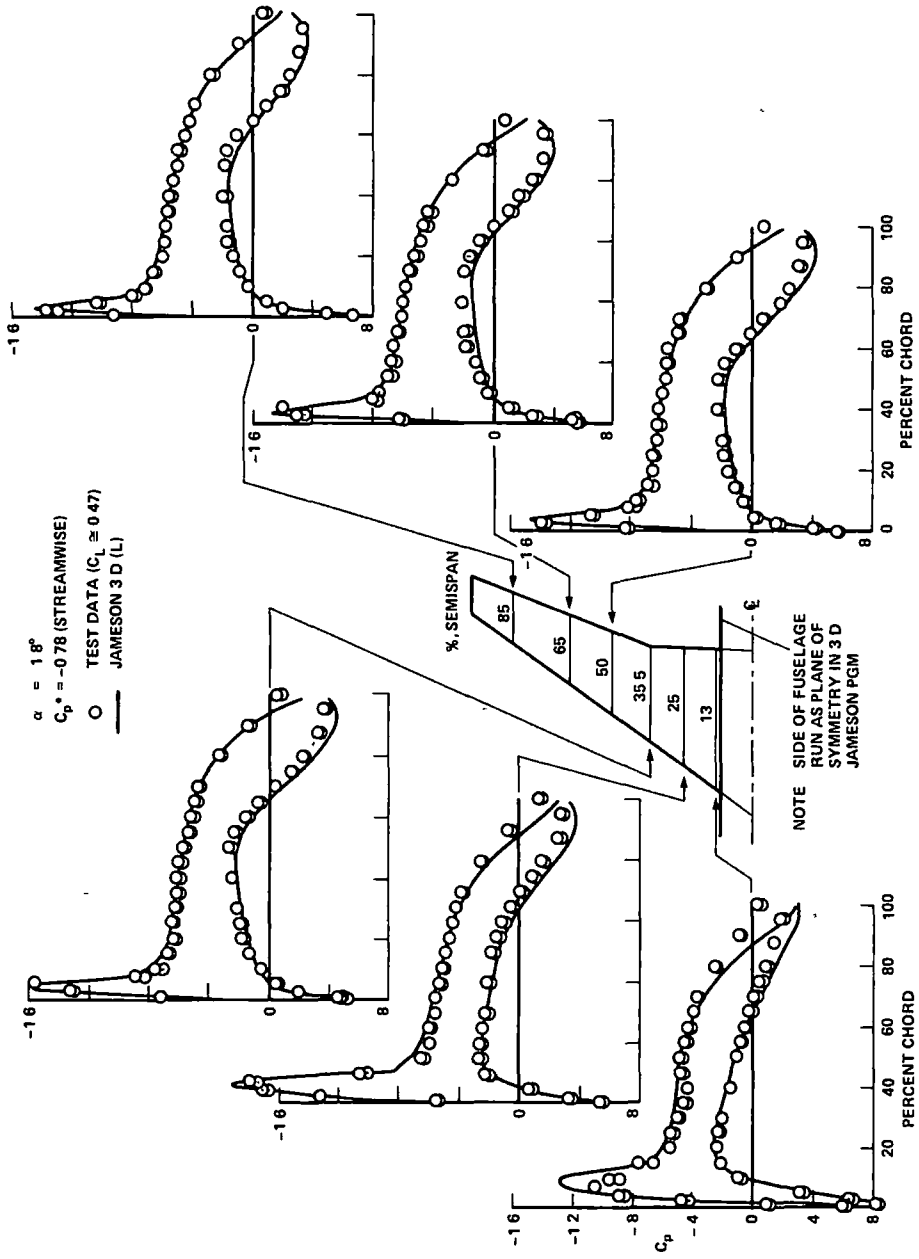
Figure 19.– Comparison of calculated and experimental wing pressure distributions for DAC case 5 at 0 7 Mach number

33
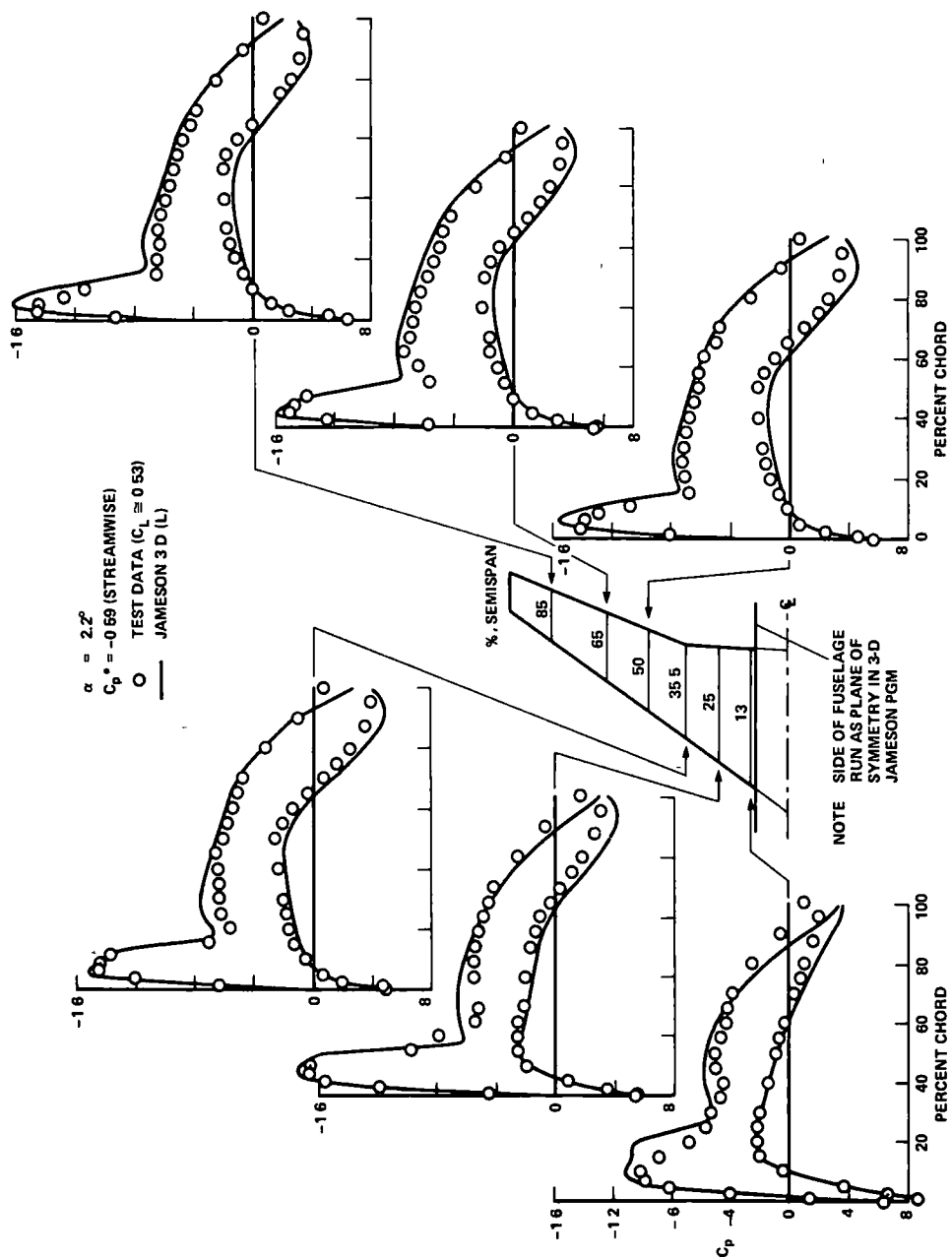
Figure 20.– Comparison of calculated and experimental wing pressure distributions for DAC case 5 at 0 75 Mach number
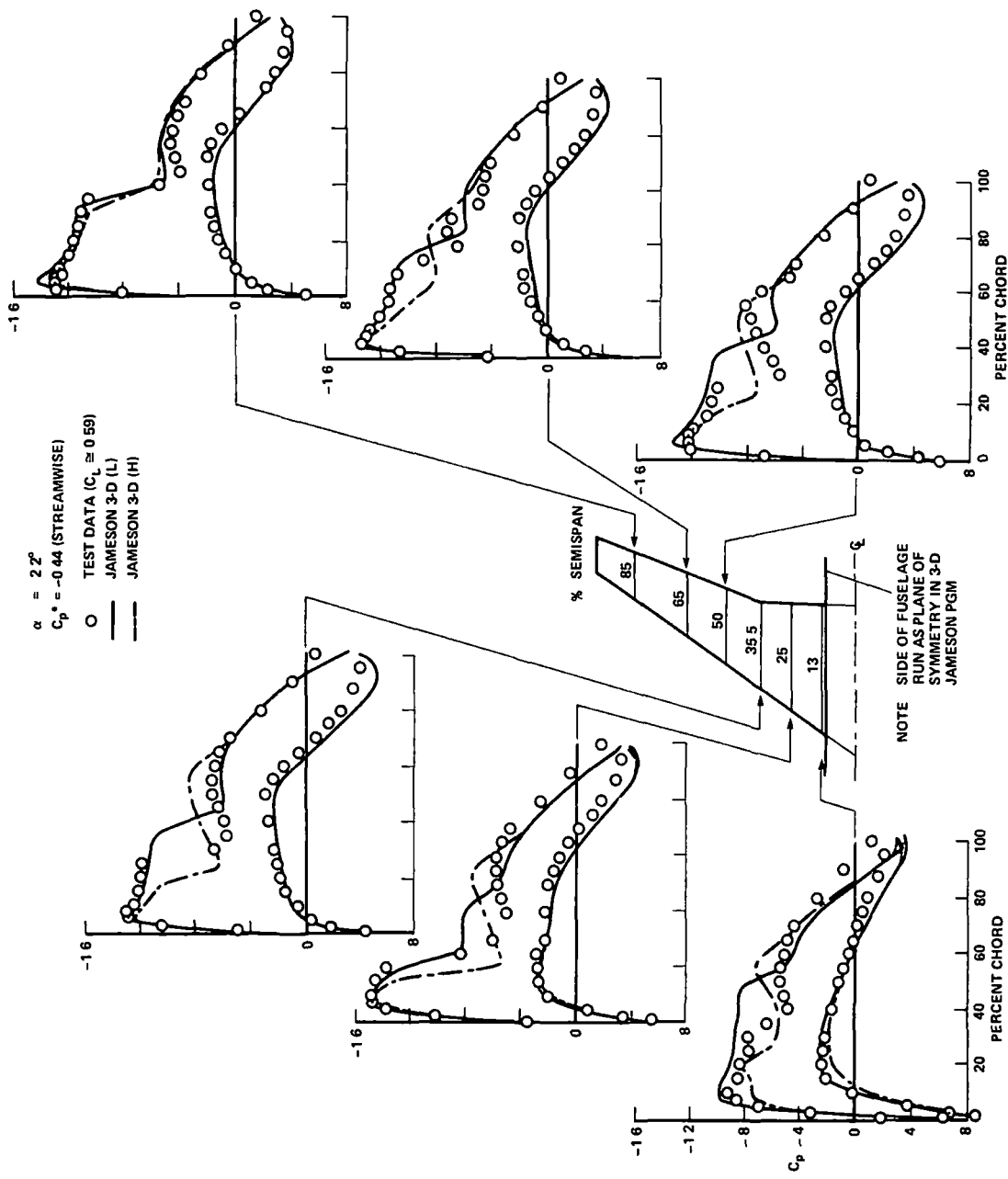
Figure 21 – Comparison of calculated and experimental wing pressure distributions for DAC case 5 at 0.8 Mach number

35
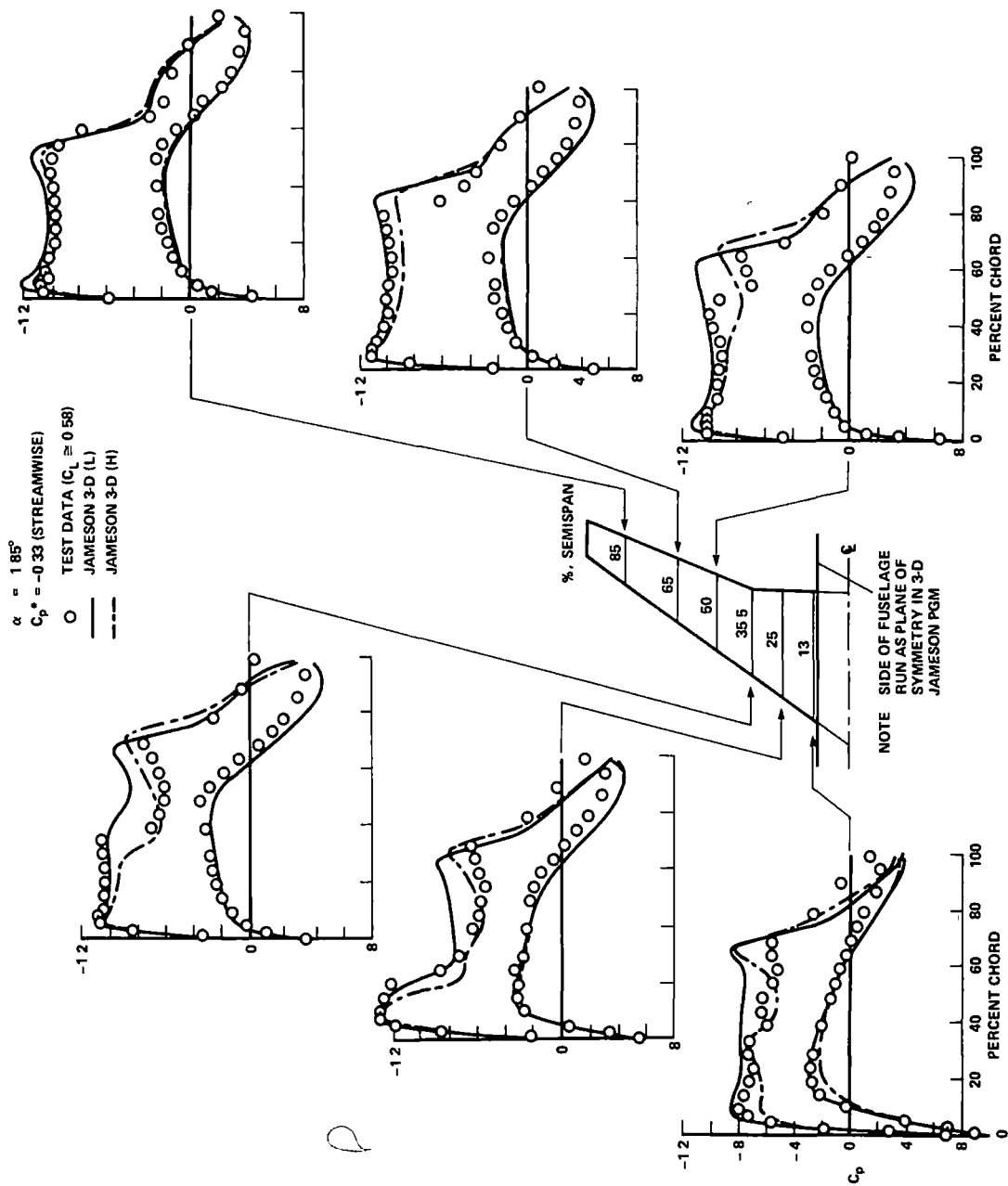
Figure 22 – Comparison of calculated and experimental wing pressure distributions for DAC case 5 at 0 84 Mach number

36
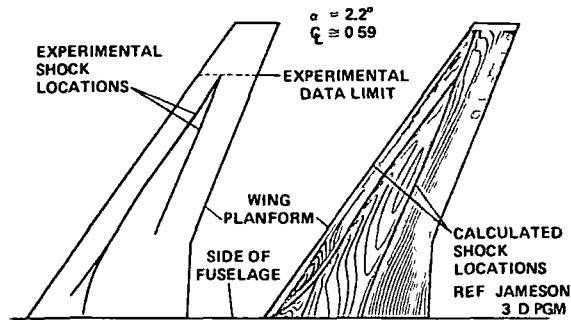
Figure 23.— Comparison of experimental and calculated shock locations for case 5 at $M_O = 0.8$
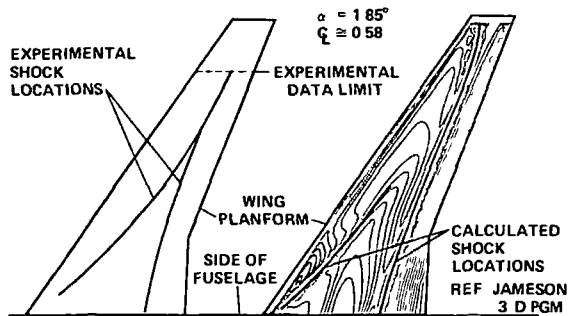
Figure 24 — Comparison of experimental and calculated shock locations for case 5 at $M_O = 0.84$
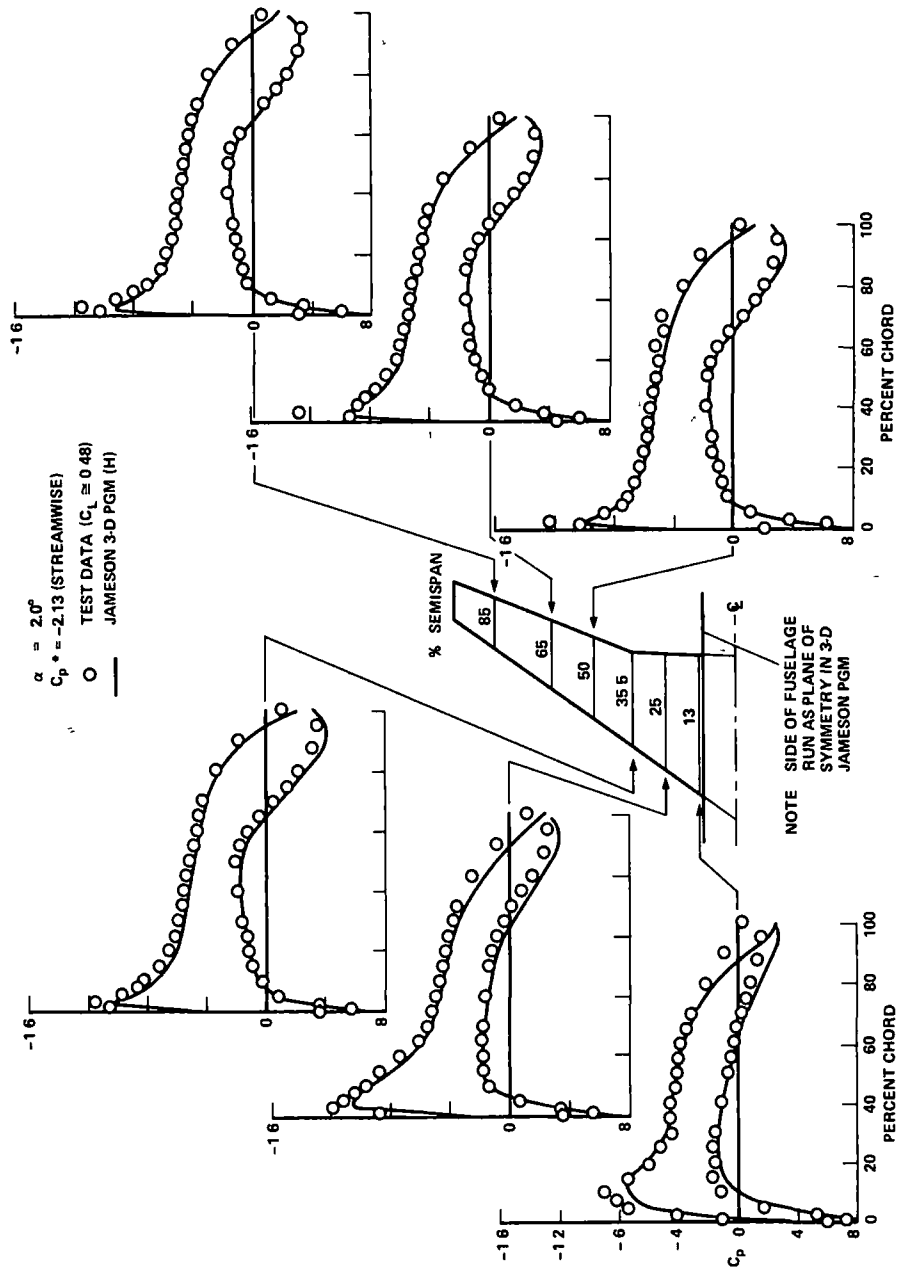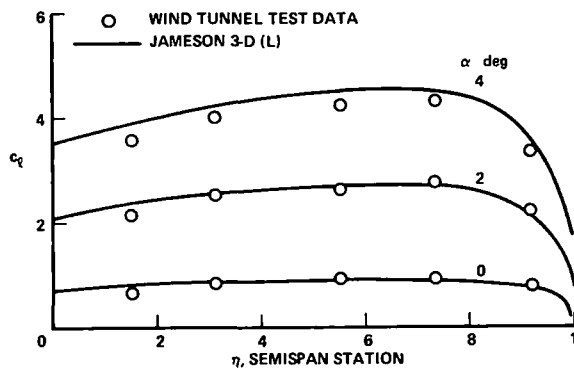
Figure 25.– Comparison of calculated and experimental wing pressure distributions for DAC case 6 at 0 5 Mach number
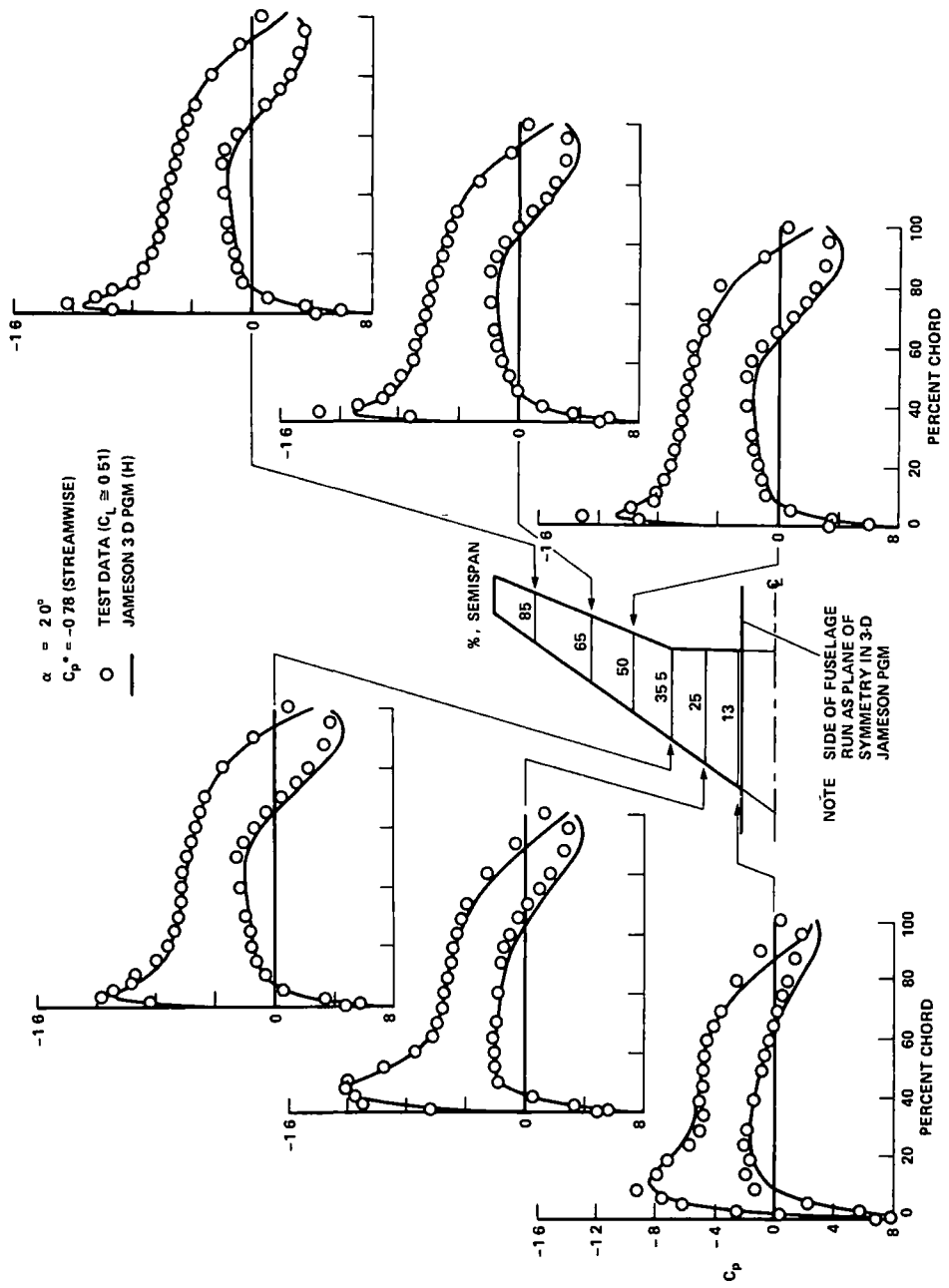
Figure 26.— Comparison of calculated and experimental wing pressure distributions for DAC case 6 at 0 7 Mach number

39
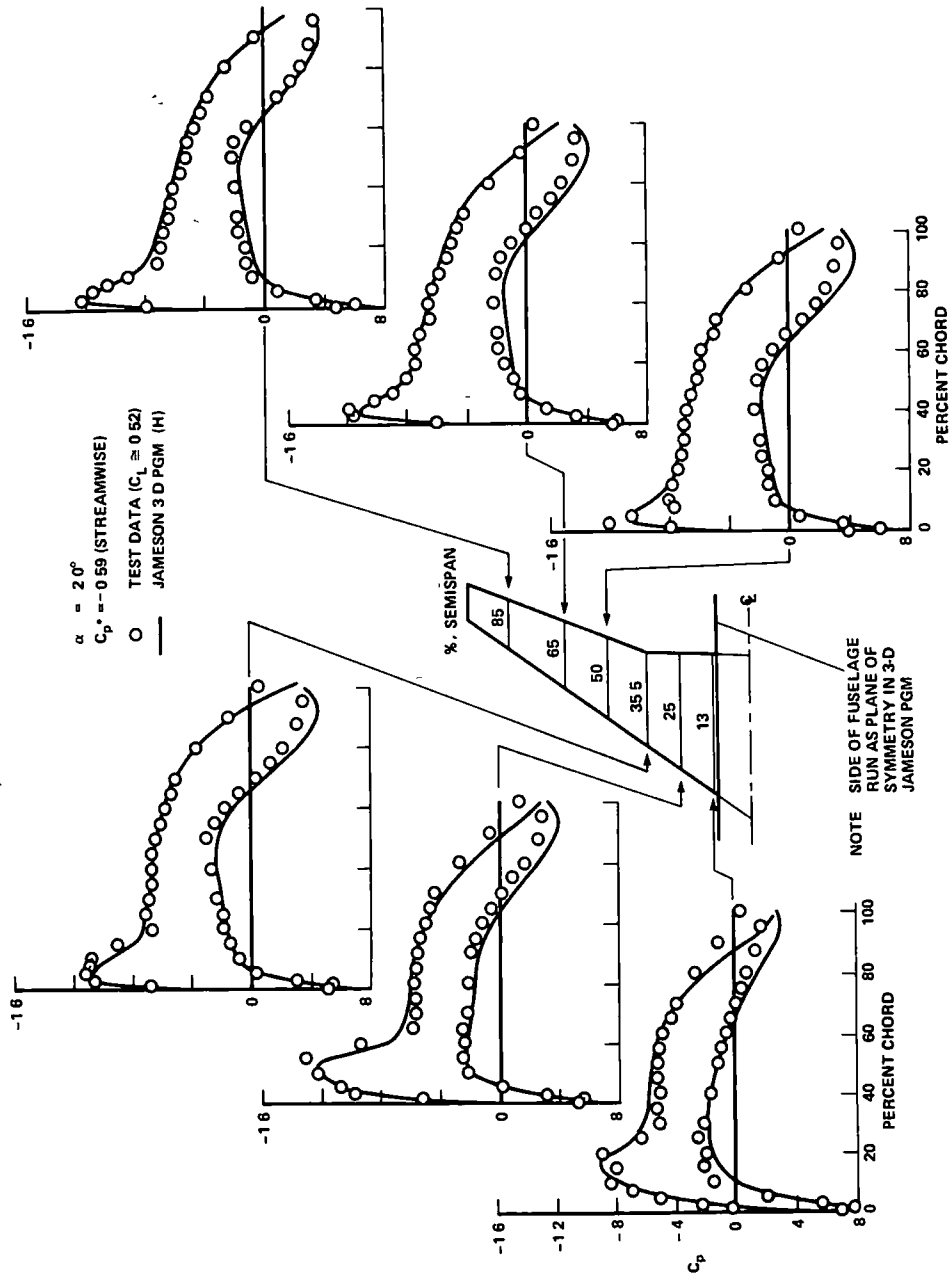
Figure 27 – Comparison of calculated and experimental wing pressure distributions for DAC case 6 at 0 75 Mach number

Figure 28 – Comparison of calculated and experimental wing pressure distributions for DAC case 6 at 0 8 Mach number

41

Figure 29 – Comparison of calculated and experimental wing pressure distributions for DAC case 6 at 0 84 Mach number

Figure 30.— Comparison of experimental and calculated shock locations for case 6 at $M_O = 0\ 8$
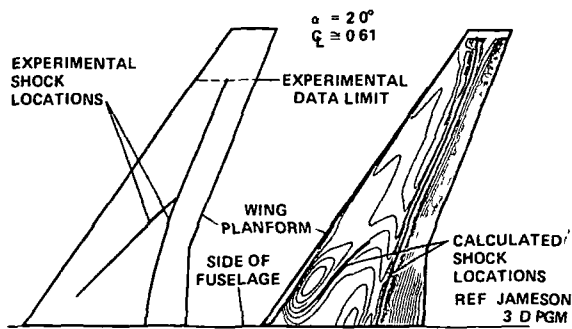
Figure 31 — Comparison of experimental and calculated shock locations for case 6 at $M_O = 0\ 84$
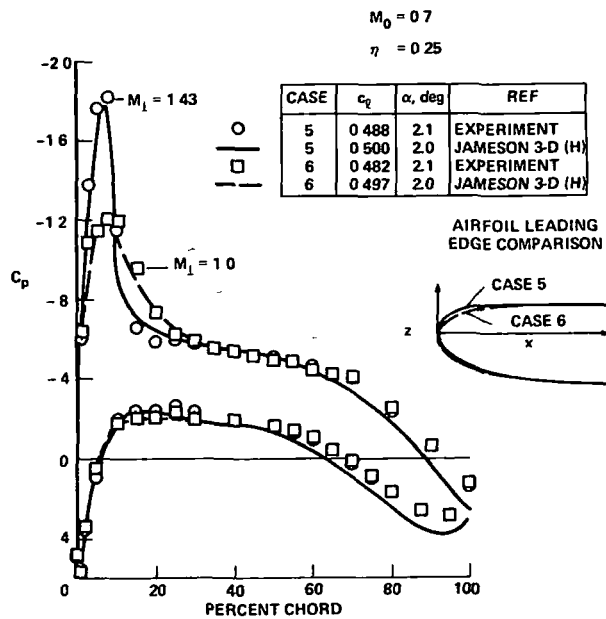
Figure 32 – Comparison of experimental pressure distributions for case 5 and case 6.
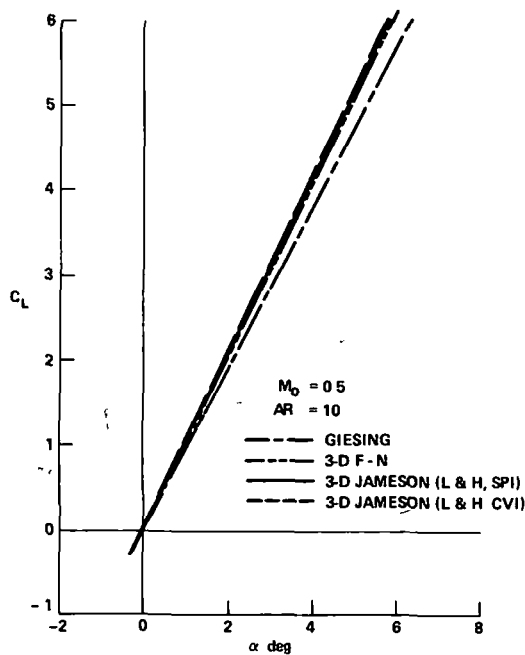
Figure 33.– Calculated lift curves for DAC case 1
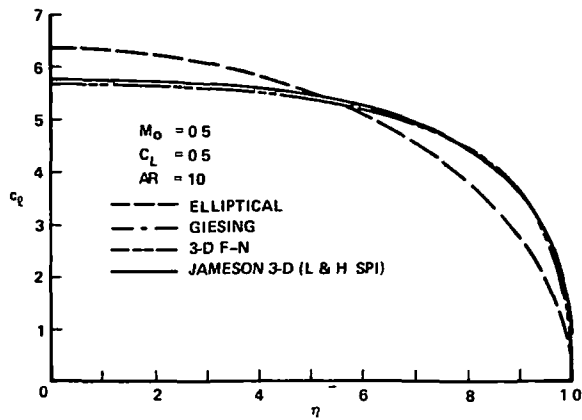
Figure 34 – Calculated spanwise distribution of section lift coefficient for DAC case 1
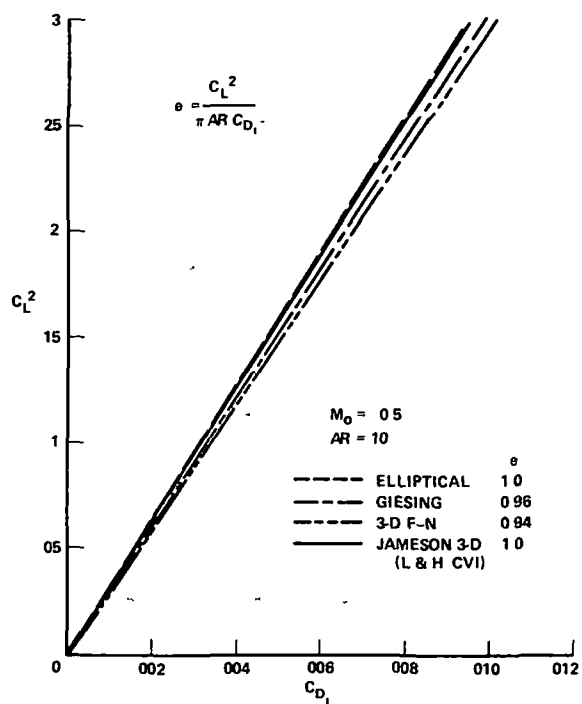
Figure 35 – Computed induced drag polars for DAC case 1
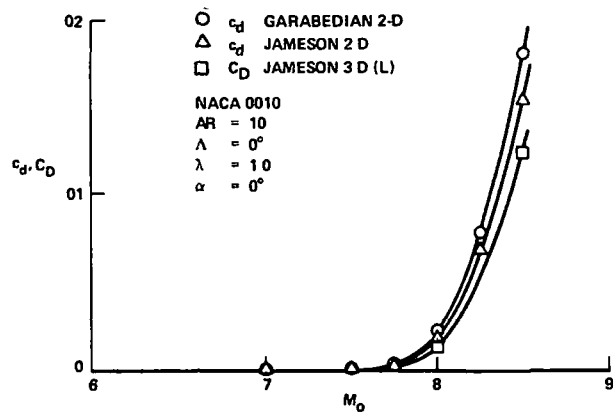
Figure 36 – Calculated shock drag rise characteristics for DAC case 1
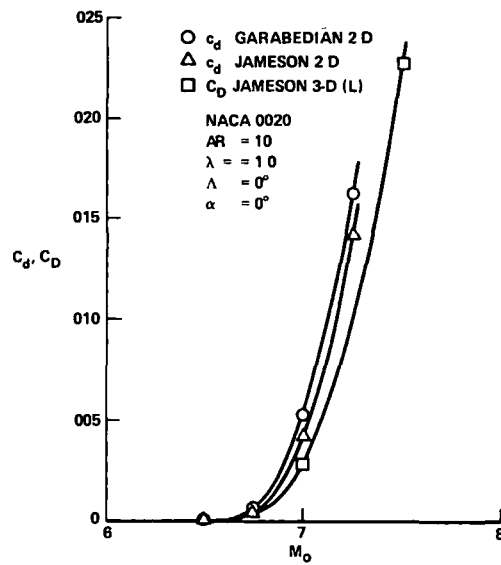
Figure 37 – Calculated shock drag rise characteristics for DAC case 2
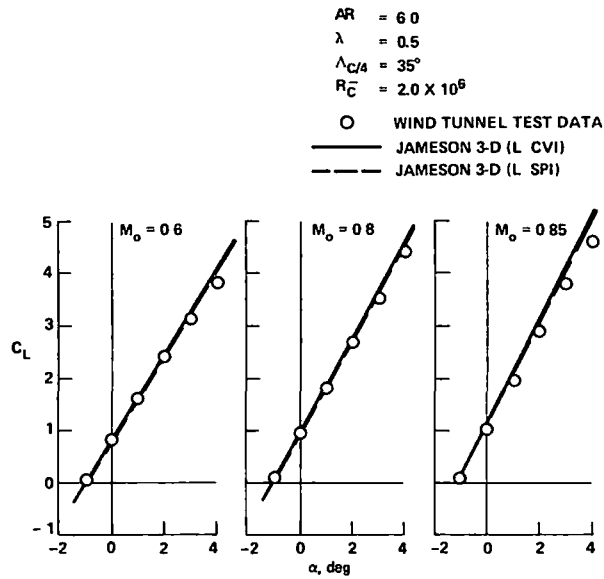
Figure 38 – Comparison of calculated and experimental lift curves for DAC case 3

Figure 39 – Comparison of calculated and experimental spanwise lift distribution for DAC case 3 at 0 6 Mach number
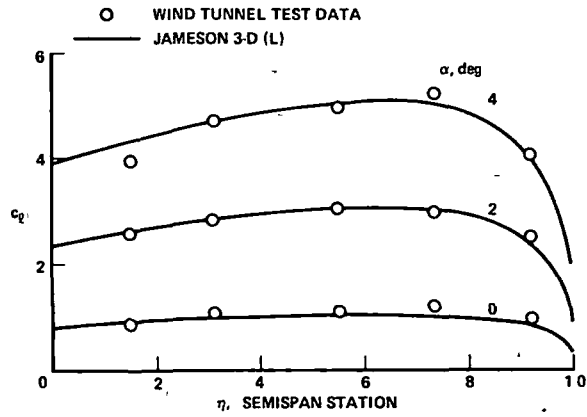
Figure 40 – Comparison of calculated and experimental spanwise lift distribution for DAC case 3 at 0.8 Mach number
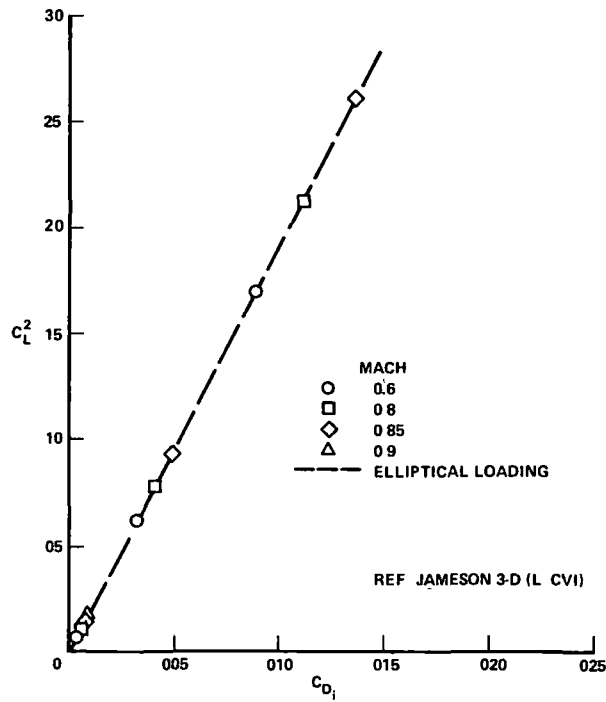
Figure 41 – Calculated induced drag polar for DAC case 3
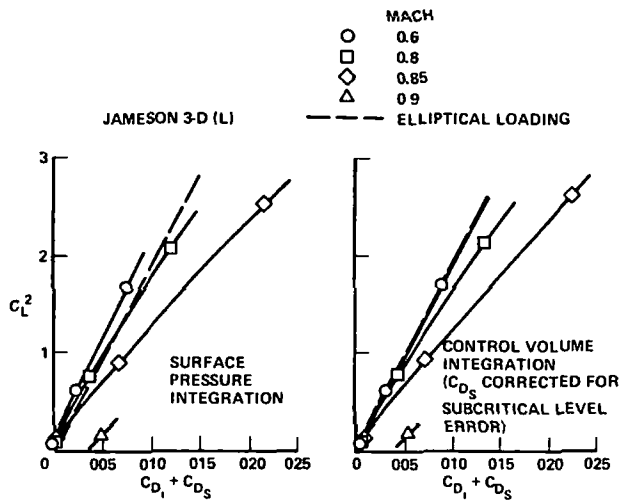
Figure 42 – Comparison of calculated drag polars using surface pressure integration and control volume integration for DAC case 3
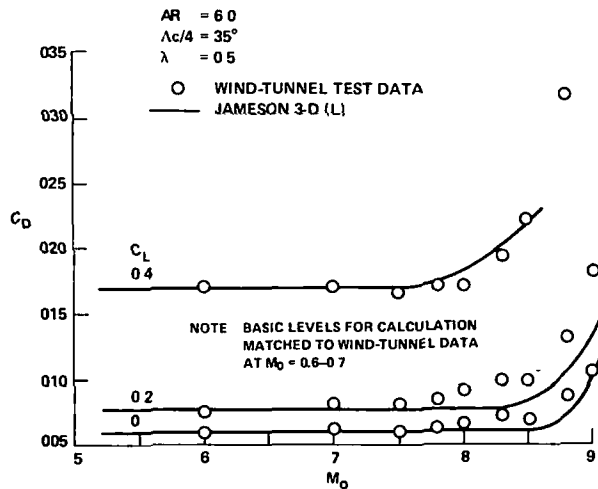
Figure 43 – Comparison of calculated and experimental drag rise characteristics for DAC case 3
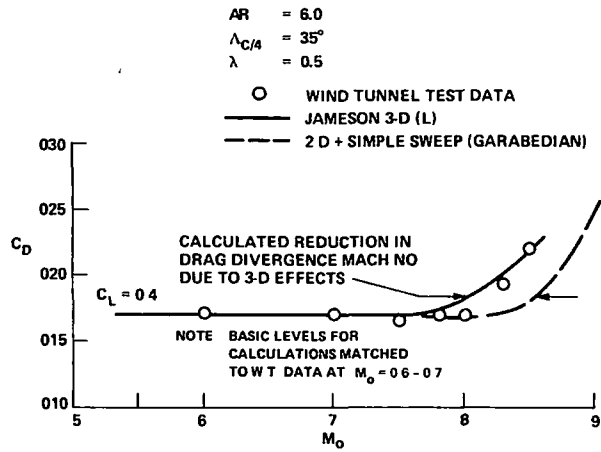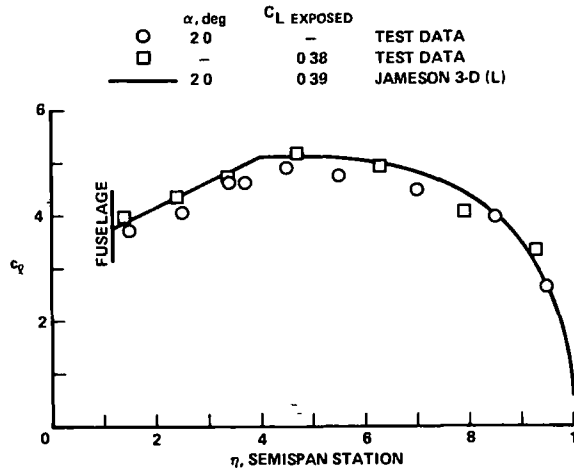
AR = 6.0
$\Lambda_{C/4}$ = 35°
λ = 0.5

○ WIND TUNNEL TEST DATA
—— JAMESON 3-D (L)
— — — 2 D + SIMPLE SWEEP (GARABEDIAN)

CALCULATED REDUCTION IN
DRAG DIVERGENCE MACH NO
DUE TO 3-D EFFECTS

C_L = 0 4

NOTE BASIC LEVELS FOR
CALCULATIONS MATCHED
TO W T DATA AT M_o = 0 6 - 0 7

C_D

M_o

Figure 44 — Estimated reduction in drag divergence Mach number due to three-dimensional effects for DAC case 3

	α, deg	C_L EXPOSED	
○	2 0	—	TEST DATA
□	—	0 38	TEST DATA
——	2 0	0 39	JAMESON 3-D (L)

FUSELAGE

c_ℓ

η, SEMISPAN STATION

Figure 45 — Comparison of calculated and experimental spanwise lift distribution for DAC case 4 at 0 85 Mach number
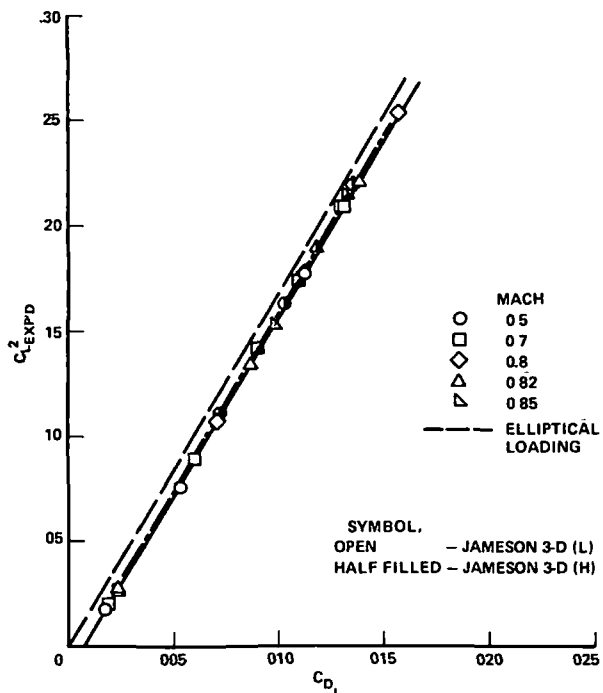
Figure 46 — Calculated induced drag polars using lower order and higher order wall boundary condition for DAC case 4
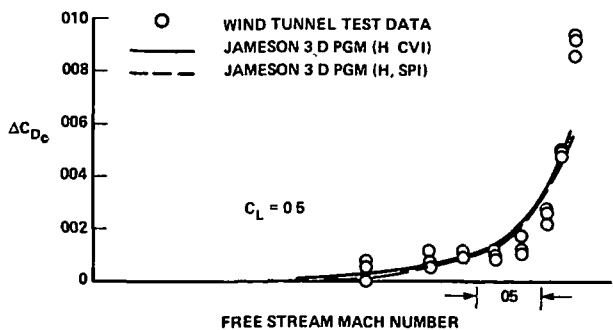

Figure 47.— Comparison of calculated and experimental drag rise characteristics for DAC case 4
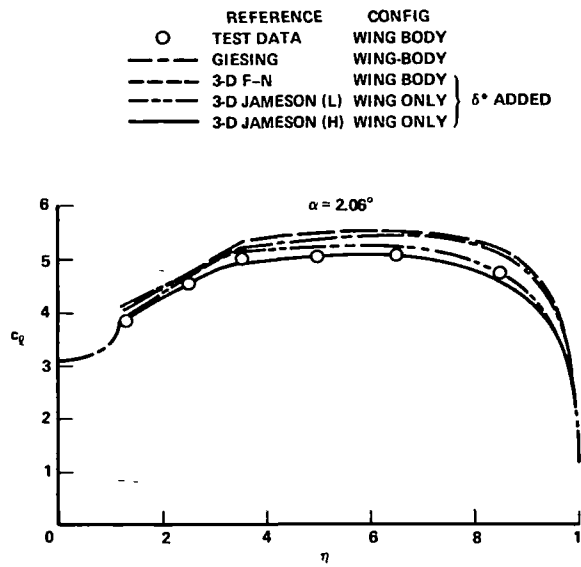
Figure 48.— Comparison of calculated and experimental spanwise lift distributions at constant α for DAC case 5 at 0 5 Mach number
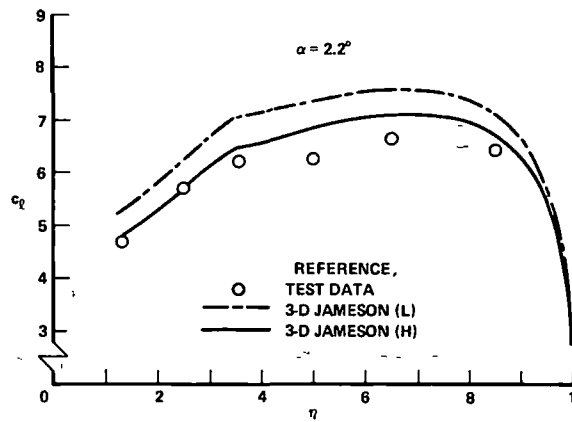

Figure 49 — Comparison of calculated and experimental spanwise lift distributions at constant α for DAC case 5 at 0 8 Mach number
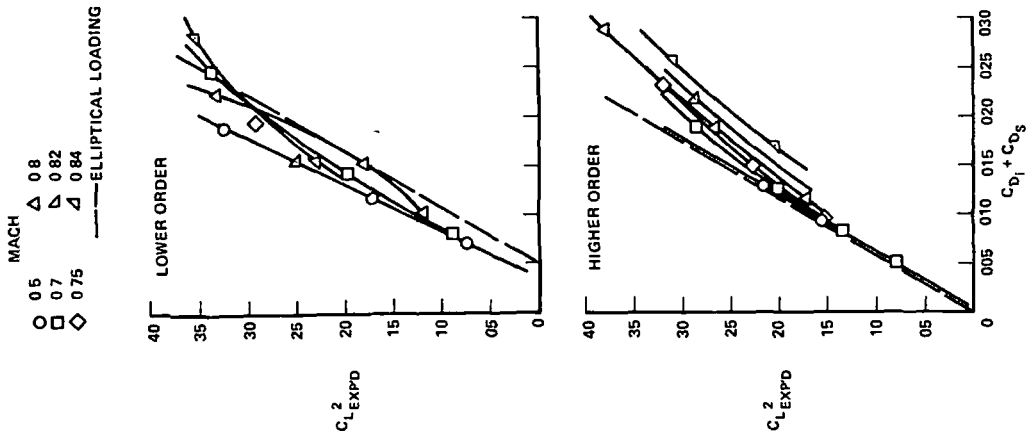
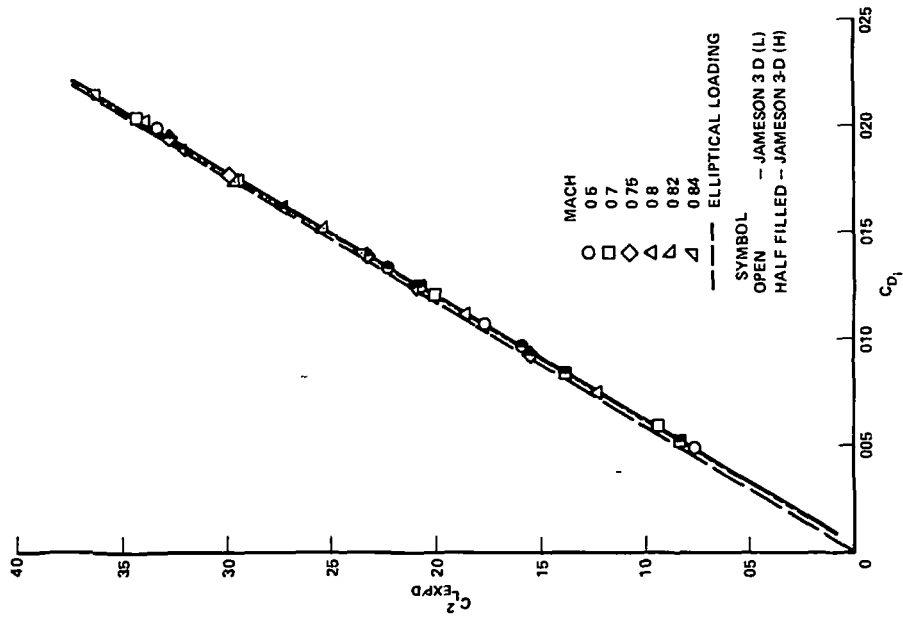Figure 51.– Computed drag polars for DAC case 5 with lower order and higher order wall boundary condition

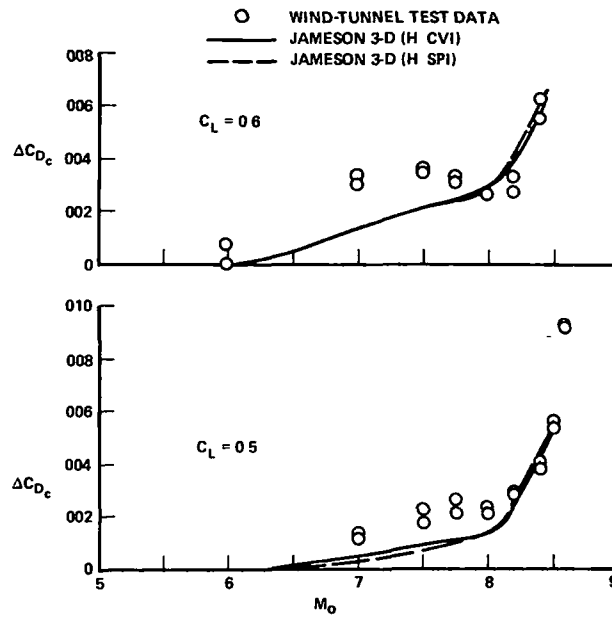Figure 50 – Calculated induced drag polars using lower order and higher order wall boundary conditions for DAC case 5

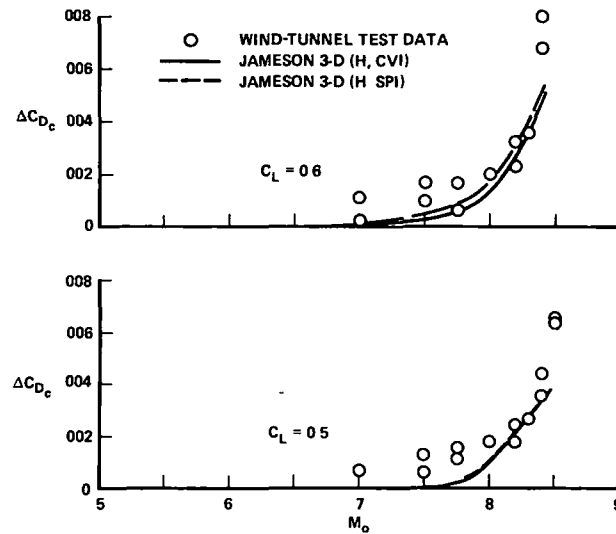Figure 52.– Comparison of calculated and experimental drag rise characteristics for DAC case 5

Figure 53 – Comparison of calculated and experimental drag rise characteristics for DAC case 6
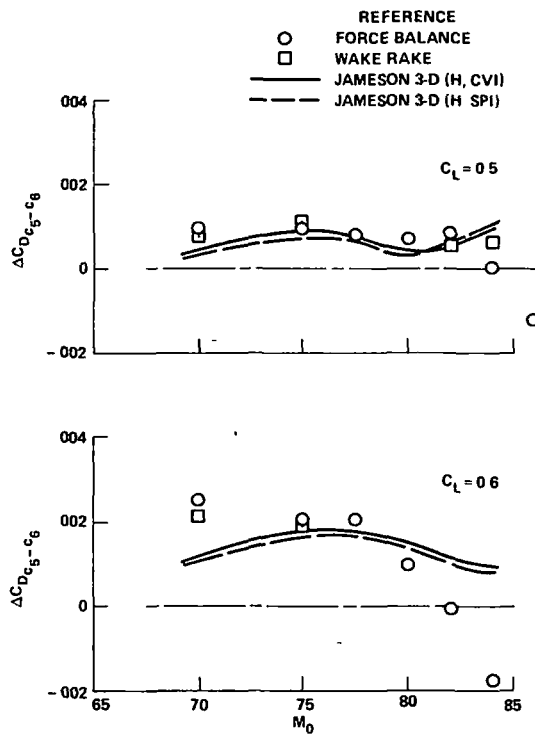
Figure 54 — Comparison of force balance, wake rake, and calculated drag increments for super-critical wings (cases 5 and 6)

1 Report No NASA TM-78464	2 Government Accession No	3 Recipient's Catalog No	
4 Title and Subtitle WING ANALYSIS USING A TRANSONIC POTENTIAL FLOW COMPUTATIONAL METHOD		5 Report Date July 1978	
		6 Performing Organization Code	
7 Author(s) P. A. Henne and R. M. Hicks		8 Performing Organization Report No A-7308	
9 Performing Organization Name and Address McDonnell Douglas Corp., Douglas Aircraft Co Long Beach, Calif. 90801 and NASA Ames Research Center Moffett Field, Calif 94035		10 Work Unit No 505-06-51-03-00	
		11 Contract or Grant No	
12 Sponsoring Agency Name and Address National Aeronautics and Space Administration Washington, D.C. 20546		13 Type of Report and Period Covered Technical Memorandum	
		14 Sponsoring Agency Code	

15 Supplementary Notes

16 Abstract

This report summarizes an evaluation of a transonic, full potential flow, computational method for wing analysis The ability of the method to compute wing transonic performance has been determined by applying the method to several different wing designs. Comparisons of computed results have been made with both experimental data and results computed by other theoretical procedures Both pressure distributions and aerodynamic forces were evaluated While some inaccuracies were discovered, comparisons indicate that the method is a significant improvement in transonic wing analysis capability. In particular, the computational method generally calculated the correct development of three-dimensional pressure distributions from subcritical to transonic conditions Complicated, multiple shocked flows observed experimentally have been reproduced computationally The ability to identify the effects of design modifications has been demonstrated both in terms of pressure distributions and shock drag characteristics. The method is applicable to a wider variety of wing configurations, since it solves the full potential equation rather than the small disturbance form of the equation.

17 Key Words (Suggested by Author(s)) Aerodynamic analysis Wing design Aircraft design	18 Distribution Statement Unlimited STAR Category – 02		
19 Security Classif (of this report) Unclassified	20 Security Classif (of this page) Unclassified	21 No of Pages 60	22 Price* $4 50

National Aeronautics and
Space Administration

Washington, D.C.
20546

THIRD-CLASS BULK RATE

Postage and Fees Paid
National Aeronautics and
Space Administration
NASA-451

NASA

on 158
Return